



HAL
open science

Modeling of chloride spatial variability in a reinforced concrete wharf from on-site measurements

Romain Clerc, Franck Schoefs, Mestapha Oumouni, Othmen Ines, Stéphanie Bonnet

► **To cite this version:**

Romain Clerc, Franck Schoefs, Mestapha Oumouni, Othmen Ines, Stéphanie Bonnet. Modeling of chloride spatial variability in a reinforced concrete wharf from on-site measurements. 2023. hal-04494998

HAL Id: hal-04494998

<https://nantes-universite.hal.science/hal-04494998>

Preprint submitted on 8 Mar 2024

HAL is a multi-disciplinary open access archive for the deposit and dissemination of scientific research documents, whether they are published or not. The documents may come from teaching and research institutions in France or abroad, or from public or private research centers.

L'archive ouverte pluridisciplinaire **HAL**, est destinée au dépôt et à la diffusion de documents scientifiques de niveau recherche, publiés ou non, émanant des établissements d'enseignement et de recherche français ou étrangers, des laboratoires publics ou privés.

1 **Modeling of chloride spatial variability in a reinforced concrete wharf from on-**
2 **site measurements**

3 **Romain CLERC**¹, **Franck SCHOEFS**¹, **Mestapha OUMOUNI**¹, **Inès**
4 **OTHMEN**², **Stéphanie BONNET**²

6 ¹ *Nantes Université, École Centrale Nantes, CNRS, GeM, UMR 6183, F-44000 Nantes, France*

7 ² *Nantes Université, École Centrale Nantes, CNRS, GeM, UMR 6183, F-44600 Saint-Nazaire,*
8 *France*

9 * Corresponding author email: franck.schoefs@univ-nantes.fr

10

11

12

13

15 Chloride ingress via diffusion is the main deterioration process of reinforced concrete (RC) structures exposed
16 to marine environment. These structures offer to the environment important lengths or surfaces. Due to the
17 material variability (different concrete batches, vibrations) and exposure variability, the material experiences
18 a spatial variability of the deterioration process. This paper presents the geostatistical analysis of in-situ
19 chloride profiles, leading to the assessment of spatial variability (SV) of both the chloride ingress itself and the
20 parameters of the widely used Fick diffusion law (the average surface chloride content, C_{sa} , and the average
21 chloride diffusion coefficient D_a). 37 chloride profiles measured on both sides of the same spandrel beam of a
22 RC wharf are studied, as well as the related estimates of C_{sa} and D_a . From an initial selection of random fields
23 models, the geostatistical analysis consists in assessing model parameters using a procedure which tests both
24 data and model assumptions on the fly (ergodicity, stationarity, random field modelling). Combined to the
25 computation of information criteria for each model, this procedure allows providing relevant geostatistical
26 models for chloride ingress, C_{sa} and D_a , which render SV as well as measurement error. It is noticeably found
27 that the error of assessment can be neglected when focusing on SV for the range of chloride content studied in
28 the paper. The SV of chloride content seems to depend on the depth, with a large variability within the
29 convection zone, and much less and more stable in the diffusion zone with a practical range of about 70cm.
30 This order of magnitude is consistent with the range of SV computed for C_{sa} (50 to 73 cm).

31 **Keywords:** Chloride ingress, Reinforced concrete, Marine environment, Spatial variability,
32 Random field, Statistical analysis.

33 **1. Introduction**

34 Chloride ingress is among the main causes of degradation of reinforced concrete (RC) structures
35 where the deterioration is more perceptible in marine environment. That leads to major maintenance
36 costs (Bastidas-Arteaga & Schoefs, 2015; Stewart & Val, 2003). These structures offer to the
37 environment important lengths or surfaces. Due to the variabilities of both the material (different
38 concrete batches, vibrations) and exposure, they experience a spatial variability of their deterioration
39 process. Accounting for realistic spatial correlation of the different parameters in structural safety
40 models may lead to more realistic estimates on structural reliability and maintenance planning,
41 knowing that reliability assessment is affected by spatial correlation (Schoefs et al., 2022; Stewart,
42 2004; Stewart & Mullard, 2007). Moreover, quantifying this property allows optimizing inspection
43 meshing on a structure (Gomez-Cardenas et al., 2015; Oumouni & Schoefs, 2021b; Schoefs et al.,

44 2017a).

45 The variability of the degradation parameters and their measurements can be described at
46 different scales:

- 47 • the point scale, characterizing the repeatability of measurements;
- 48 • the local scale of the material, characterizing the heterogeneity of the material for a scale
49 lower than the Representative Elementary Volumes (REV) associated with each of the
50 quantities of interest (Hill, 1963);
- 51 • higher scales (structural elements, structure), characterizing the degree of spatial
52 heterogeneity of the material and/or environmental conditions (exposure, loading, ...) for
53 scales above the REVs.

54 The restitution of point and local variabilities requires a statistical modeling, translating the
55 hypothesis of independence, respectively on (i) the measurements of parameters between distinct
56 measurements and for a same measurement point and (ii) the parameter values between similar
57 structures for the same REV dimension. The spatial variability (taking into account local and larger
58 scales) cannot be solely captured by a statistical modelling because of the hypothesis of the existence
59 of a certain degree of heterogeneity, i.e. spatial correlation, between measurements or between
60 parameter values associated with different measurement points or REV on the same structure. This
61 can only be translated by geostatistical modeling. The major challenge of those models is to determine
62 stochastic properties of the Random Fields (RF), namely their marginal distributions, stationarity and
63 the spatial correlations.

64 Chloride ingress has been investigated deeply since the 70's and it has been shown how
65 complex is the process physically and chemically (Glasser et al., 2008; Kaushik & Islam, 1995; Ragab
66 et al., 2016; Safhi et al., 2019; Wegian, 2010) and the role the material complexity (porosity) is
67 playing (Qu et al., 2021). For the moment, available models of transfer and knowledge don't allow

68 to represent accurately the spatial variability of pollutant in concrete (Ravahatra et al., 2017). That is
69 the main reason why direct or indirect assessment of chlorides in situ is the only way to measure,
70 analyze and model the spatial variability of chloride ingress. Then, two kinds of quantities of interest
71 can be considered:

- 72 • the total chloride content C at several depths;
- 73 • their mean diffusion parameters C_{sa} and D_a , estimated from profiles of chloride content.

74 During the last decades sensors have experiences significant progresses (Biondi et al., 2021;
75 Torres-Luque et al., 2014, 2017; Watanabe et al., 2021; Zaki et al., 2015) but there are few concepts
76 that measure the spatial distribution of chloride ingress (Fares et al., 2018; Lecieux et al., 2015, 2019)
77 and their implementation is rare (Priou et al., 2019) even if their interest in terms of the value of
78 information they provide was shown (Schoefs et al., 2022) especially because they allow to filter the
79 signal (Oumouni & Schoefs, 2021a). Moreover, these sensors have to be installed at the building
80 stage and are not suitable for existing structures.

81 That is the main reason why spatial variability is assessed through Non-Destructive Testing
82 (NDT) tools or Semi-Destructive Techniques (SDT). On-site indirect assessment of chlorides through
83 NDT-techniques is affected by errors of assessment and sensitivity to other parameters (humidity,
84 temperature) which makes it difficult to assess the spatial variability of chlorides (Bonnet et al., 2017;
85 Bourreau et al., 2019; Schoefs et al., 2023). This error affects the optimization of measurements for
86 assessing spatial variability (Oumouni & Schoefs, 2021b). That is why, the rare studies are based on
87 the semi destructive techniques (SDT) i.e. direct weighting of chlorides from cores (O'Connor &
88 Kenshel, 2013; Othmen et al., 2018) reviewed 10 published studies from 2004 to 2016 with only 3
89 concerning more than 30 measurements and in all cases the distance between measurement was too
90 large in view to assess the spatial correlation. Two main quantities of interest are investigated:
91 chloride content at a given depth and parameters of a model of chloride ingress after post-processing
92 of chloride profiles.

93 Because of the complexity and cost for making a large amount of cores in a beam, only a few
94 amounts of data is available for each and the distance between cores is too large: 5 cores with a
95 distance of about 1 m in the study of (O'Connor & Kenshel, 2013). That leads to a significant
96 numerical error of assessment of the spatial correlation (Schoefs et al., 2017b). Moreover, the
97 underlying assumptions for RF modelling that are stationarity and ergodicity are not checked. Finally,
98 the error of measurement is usually not considered when identifying correlations. That is a drawback
99 because it is well known that SDT measurements for existing structures (Schoefs et al., 2023) and
100 even for concrete in laboratory (Bonnet et al., 2017; Hunkeler et al., 2000) are affected by a significant
101 error. To overcome these limits, this paper relies on two pillars: first, a unique database and second,
102 a geostatistical analysis that allows to provide geostatistical parameters (namely spatial correlation
103 assessments as well as measurement error) by using a recent method of RF identification (SCAP1D,
104 Clerc et al. 2019), that accounts for uncertainty of measurements, checks ergodicity and accounts for
105 the non-stationarity of the RF.

106 Concerning the first pillar, marine structures can be exposed in various environments:
107 atmospheric, spatter or splash, tidal and underwater (BS 6349-1:2000, 2000) which were defined
108 according to the tide range (Bourreau et al., 2020). In this work, 30 cores carried out every 30 cm on
109 the same 28-year beam (Othmen et al., 2018) are analyzed. The beam is located in the worst
110 environment that is splash zone (Angst et al., 2009), and the cores are through its width giving access
111 to profiles from each side i.e., exposure conditions (exposed, sheltered).

112 Concerning the second pillar, two objectives are targeted: the assessment of spatial variability
113 of the total chloride content C , depending on depth and exposure on one hand and the assessment of
114 the spatial variability of the mean diffusion parameters C_{sa} and D_a on the second one. First, taking
115 benefit of the availability of C at several depth, the objective is to provide estimates of its geostatistical
116 parameters and to answer the following questions: (i) Is the spatial variability (SV) of C a function of
117 depth? (ii) Is the SV of C a function of the exposure conditions? Second, knowing the age of the
118 structure (28-year), geostatistical parameters of mean diffusion parameters are estimated to answer

119 the following question: Is the SV of C_{sa} and D_a a function of the exposure conditions? The latter
120 question arises because C_{sa} and D_a are directly dependent on the chloride profiles, which vary
121 markedly between the exposed and sheltered faces.

122 Section 2 introduces the geostatistical formalism in a theoretical way before presenting a state
123 of the art of RF modeling, simulation methods and spatial variability estimation methods. An attention
124 is paid to the underlying assumptions of the estimation methods and to the consequences of their
125 neglect on the estimated spatial variability, especially in the frequent case of non-stationary
126 measurements due to spatially variable exposure conditions. Section 3 presents the structure and the
127 available data. Sections 4 and 5 give the results at two levels: total chloride contents, and mean
128 diffusion parameters of total chlorides. Section 6 concludes the paper with some extension to other
129 structures or other exposures.

130 **2. Geostatistical methods for spatial variability assessment of concrete structures**

131 **2.1. Modelling of spatial variability**

132 *2.1.1. Random Field modeling*

133 Practical modelling of spatial variability implies to model spatially variable quantity of interest (q.i)
134 as Second Order Intrinsic Stationary Random Fields (RF) (Chilès & Delfiner, 2012). Following
135 geostatistical formalism, such a RF Z is defined on a domain D of \mathbb{R}^n and on a probability space
136 (Ω, A, P) such that:

- 137 • $\forall \mathbf{x} \in D^n$ and $\forall (p, q) \in [1; n]^2$, $Z(\mathbf{x}, \cdot) = Z_{\mathbf{x}}$ is a multivariate random variable of $\omega \in \Omega$ with joint
138 probability density function (pdf) $f_Z(\mathbf{m}, \Sigma)$;
- 139 • $\forall \mathbf{x} \in D^n$ and $\forall \omega \in \Omega$, $Z(\mathbf{x}, \omega) = Z_{\mathbf{x}}^{\omega}$ is a realization of Z georeferenced by vector \mathbf{x} , also called
140 *trajectory* (in practice, one set of measurements from a unique structure and at a unique time).
- 141 • $\forall (h, \mathbf{x}) \in D^2$, $\mathbb{E}[Z_{\mathbf{x}+h} - Z_{\mathbf{x}}] = 0$ and $Var(Z_{\mathbf{x}+h} - Z_{\mathbf{x}}) = 2\gamma(h)$ with $\gamma(\cdot)$ the *semi-variogram* of
142 Z and h any space lag;

143 This definition reflects both the variability of input parameter between structures and its spatial
 144 variability within the same structure, which are embedded into the *covariance matrix* Σ and the semi-
 145 variogram.

146 In this paper, data are modeled as (i) unidimensional (ii) noisy (iii) trend-stationary (iv) Gaussian
 147 Random Field (GRF). Indeed, (i) data are unidimensional along beam sides; (ii) if the spacing
 148 between measurements is larger than the REV, the RF model must be able to reproduce the point and
 149 local variabilities, which do not have a correlation structure and can be modeled by white noise; (iii)
 150 materials and environmental conditions may vary along beam sides. It is then highly probable that
 151 the mean of the quantities of interest varies with space; (iv) GRF are very handy as they allow to
 152 model most natural variabilities (following normal or lognormal marginal laws) with only a model
 153 for the mean and the covariance (Chilès & Delfiner, 2012).

154 Mathematically, $\forall \mathbf{x} \in D^n$ we thus consider Z such that

$$Z_{\mathbf{x}} = \mathbf{m}_{\mathbf{x}} + W_{\mathbf{x}} + Y_{\mathbf{x}} \quad (1)$$

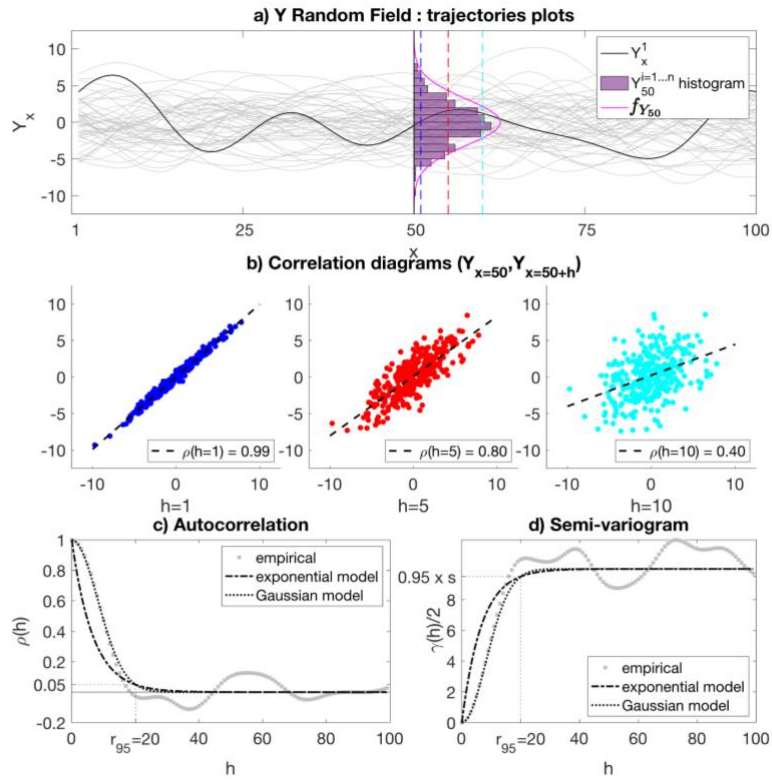
155 With $\mathbf{m}_{\mathbf{x}}$ a deterministic trend, $W_{\mathbf{x}} \sim N(\mathbf{0}, t \times \mathbf{1}_n)$ a white noise of variance t ; $Y_{\mathbf{x}} \sim N(\mathbf{0}, \Sigma_Y)$ a
 156 centered GRF, i.e $Y_{\mathbf{x}}$ a multivariate normal variable such that

$$\forall (h, \mathbf{x}) \in D^2, \Sigma_{Y_{\mathbf{x}+h}, Y_{\mathbf{x}}} \equiv Cov(Y_{\mathbf{x}+h}, Y_{\mathbf{x}}) \equiv C_Y(h) \equiv s \times \rho_Y(h) \quad (2)$$

157 with $C_Y(\cdot)$ the covariance function of Y , s its variance, $\rho_Y(\cdot)$ its autocorrelation function, and h any
 158 distance-lag between data (equivalences due to the Second Order Stationarity of GRF).

159 This formalism is illustrated on Figure 1 and Figure 2, where trajectories, correlation diagrams,
 160 autocorrelation functions and semi-variograms are plotted for Y and Z respectively, defined such that

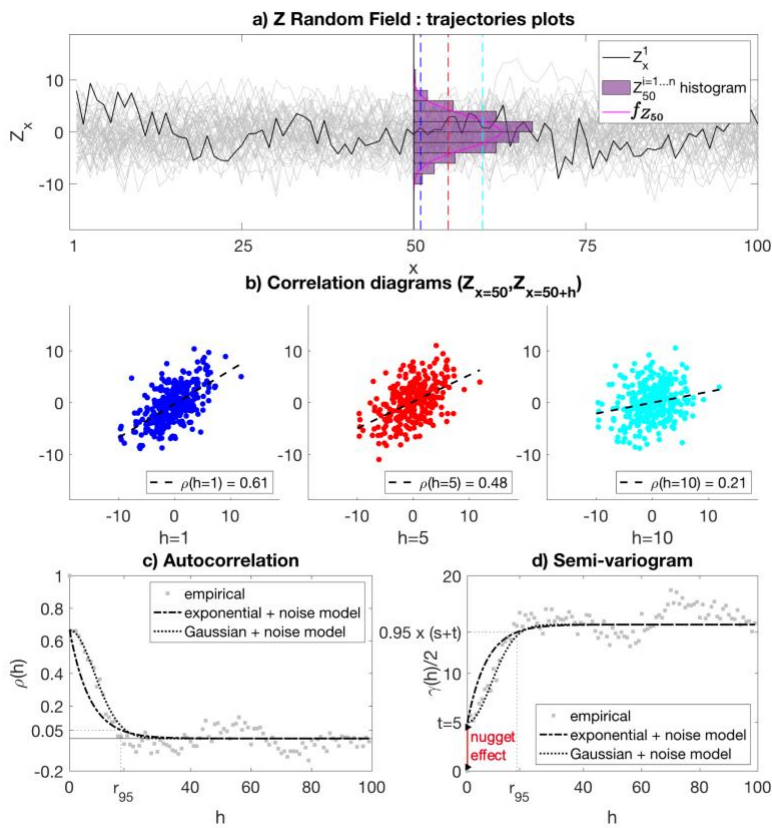
161 (1) $Y_{\mathbf{x}} \sim N(\mathbf{0}, \Sigma_Y)$ with $\Sigma_{Y_{\mathbf{x}+h}, Y_{\mathbf{x}}} = s \times \exp(-1.73\|h\|^2/r_{95})$, $s = 10$ and $r_{95} = 20$, and (2) $Z = W +$
 162 Y with $W_{\mathbf{x}} \sim N(\mathbf{0}, t \times \mathbf{1}_n)$ and $t = 5$.



163

164

Figure 1 - Illustration of the geostatistical formalism: GRF Y



165

166

167

Figure 2 - Illustration of the geostatistical formalism: noisy GRF Z

168 2.1.2. Autocorrelation models and parameters

169 Table 1 and Figure 1 respectively presents and illustrates the exponential and Gaussian
 170 autocorrelation functions, widely used in the literature. In accordance with Equation (2) such
 171 functions are positive definite such that they asymptotically decrease as a function of the distance-lag
 172 h . The evolution of this decay is mainly driven by the value of their scale parameter $a > 0$, which
 173 parametrizes the extent of the spatial correlation, i.e. the spacing threshold below which the q.i are
 174 strongly correlated.

175 The distance for which events are weakly correlated is called the Inspection Distance Threshold with
 176 a definition of a Spatial Correlation Threshold of 30% in (Schoefs et al., 2016). Several notations and
 177 parameters coexist in the literature to describe this threshold, sometimes with some confusion. In the
 178 case of isotropic fields, (i) Cressie (1993, p. 118) defines the fluctuation range θ , such that $\theta =$
 179 $\int_{-\infty}^{+\infty} \rho(h)dh$; (ii) the same author (p. 88) defines by the practical range r_{95} , such that $\rho(r_{95}) = 5\%$
 180 (see Figure 1 and Figure 2) and (iii) the correlation length l_c is not strictly defined and alternatively
 181 taken equal to a , θ , r_{95} or any other particular range. In order to avoid any confusion and to simplify
 182 comparison and interpretations, we specify in Table 1 the expression of θ and r_{95} as a function of a
 183 for the exponential and Gaussian models and the associated autocorrelation values ρ . Note that on
 184 Figure 1 Y is obtained from a Gaussian autocorrelation function.

185 *Table 1 - Exponential and Gaussian autocorrelation functions, and relations between their scale parameter,*
 186 *fluctuation scale and practical range*

Name	Model	θ	$\rho(h = \theta)$	r_{95}	$\rho(h = r_{95})$
exponential	$\rho(h) = \exp(-\ h\ /a)$	$2a$	0.135	$3a$	0.05
Gaussian	$\rho(h) = \exp(-\ h\ ^2/a)$	$\sqrt{\pi}a$	0.043	$1.73a$	0.05

a : scale parameter; θ : fluctuation parameter; r_{95} : practical range;
 $\rho(\cdot)$: autocorrelation function

188 2.2. Identification of spatial variability from measurements

189 2.2.1. Empirical identification

190 RF models behind a trajectory can be identified in case of its *ergodicity*, which can be seen as a
191 mixture of stationarity and asymptotic independence. In that case, special variability can be assessed
192 from empirical representations of the semi-variogram, the covariance function, or the autocorrelation
193 function, respectively called empirical semi-variogram, covariogram and autocorrelogram.

194 Semi-variogram, noted $\hat{\gamma}(h)$, is used as its estimate does not require supplementary ones (like mean
195 or variance), and it allows to visually identify (i) Second-Order Stationarity property, (ii) ergodicity
196 property, and (iii) presence and magnitude of local variabilities. Indeed, (i) $\hat{\gamma}(h)$ asymptotically tends
197 toward variance for Second-Order Stationary RF whereas it increases with h otherwise; (ii) ergodicity
198 is verified if $\hat{\gamma}(h)$ reaches an asymptote in the limit of half of the domain D (Cressie, 1993, p. 57);
199 (iii) white noise is easily identified by a *nugget effect*, i.e a non-zero value for $h = 0$ (see Figure 2)

200 Common estimator of $\hat{\gamma}(h)$ is defined by Equation (3) for a given trajectory Z_x^ω , where S_h is the set
201 of pairs (x_p, x_q) of D^2 distant from h modulo a given tolerance and N_h is the cardinal of S_h .

$$\hat{\gamma}(h) = \frac{1}{2N_h} \sum_{(x_p, x_q) \in S_h} (Z_{x_p}^\omega - Z_{x_q}^\omega)^2 \quad (3)$$

202 We point out that when h becomes close to the dimension of D , statistical inference is no longer
203 valid because the number of pairs of points distant from h is very small. Therefore, geostatisticians
204 recommend plotting this graph only for spacings h such that $N_h \geq 30$ (Cressie, 1993). In practice,
205 in Civil Engineering, several authors recommend limiting to values of h less than half of the size of
206 the domain (Arnaud & Emery, 2000, Schoefs et al., 2016).

207 2.2.2. Estimates of model parameters

208 Once a RF model is chosen from empirical identification, parameters \mathbf{p} have to be estimated. Several
209 methods are available:

- 210 • Maximum Likelihood Estimation (MLE), which allows to estimate \mathbf{p} from raw data given a RF
211 marginal distribution model, and as the following properties: (i) asymptotically unbiased, (ii)
212 consistent, (iii) equivariant, (iv) asymptotically efficient, and (v) asymptotically normal
213 (Wasserman, 2004, para. 9.4);
- 214 • Least-Square Estimate (LSE), which allows to estimate \mathbf{p} from semi-variogram, covariogram or
215 autocorrelogram given models of these;
- 216 • Weighted LSE (wLSE), similar to LSE, each of the residues being weighted by its variance. This
217 allows increasing the weight of the residuals computed from many data (low distance-lag h
218 values, for which N_h is greater).

219 Usually, LSE and wLSE fit well the covariograms and the use of wLSE implies a better description
220 of these for small spacing, associated with more data¹. However, covariograms are not necessarily
221 representative of the effective covariance parameters of the field, which can lead to significant relative
222 errors in their estimation. Because it only considers raw data, MLE provides more accurate estimates,
223 with smaller relative errors. The counterpart is the computation time, since MLE is more time-
224 consuming than wLSE and LSE, up to 10 times faster. Thus, and since it is *a priori* complex to have
225 an initial idea of the scale parameter, a two-phase estimation method of Second-Order Stationary RF
226 parameters is preferred:

- 227 1. wLSE pre-estimation of the parameters with the following initial values: (i) for s , the empirical
228 variance; (ii) for α , a value such that the fluctuation scale is less than a quarter of the maximum
229 lag-distance (so as to respect the ergodic assumption);
- 230 2. MLE estimation of the parameters with wLSE estimates as initial values.

231 This approach allows to obtain accurate estimates while minimizing the cost of the MLE due to the
232 definition of initial values close to the real values of the parameters (Clerc et al., 2019, para. 4.4).

¹ In this case $\gamma(h) = 1 - C(h)$, so estimates on covariogram or semi-variogram are equivalent.

233 2.2.3. *Choice of best RF model*

234 Although plotting empirical semi-variogram allows to choose a RF model, its estimator nature
 235 induces an imperfect representation of the SV. This is all the truer when the number of measurements
 236 is small. Thus, when there is insufficient scientific evidence to support a specific RF model for a q.i,
 237 which is the case for chloride content and diffusion parameters (Gomez-Cardenas et al., 2015), we
 238 can rely on data-based methods of model choice.

239 In the following, the Akaike information criterion (AIC) is preferred, as it is much more robust than
 240 the R^2 coefficient of determination (Burnham & Anderson, 2010). The AIC allows to compare, with
 241 the parsimony criterion, the relevance of any RF model M_Z with K parameters $p_{1,\dots,K}$ to describe the
 242 hidden RF Z at the origin of a set of n data Z_x^ω (for example a trajectory). This criterion assumes that
 243 the best model is the one that allows the most accurate description with the fewest possible parameters
 244 (Burnham & Anderson, 2010, para. 1.4).

245 When $n/K < 40$ and (which is the case hereafter) we use in particular the corrected information
 246 criterion (AICc). When \mathbf{p} estimate $\hat{\mathbf{p}}$ is computed with MLE, it writes:

247
$$AIC_c = \underbrace{-2 \ln(L(\hat{\mathbf{p}}|Z_x^\omega))}_{AIC} + 2K + \underbrace{\frac{2K(K+1)}{n-K-1}}_{\text{correction}}$$

248 With $L(\hat{\mathbf{p}}|Z_x^\omega)$ the likelihood of $\hat{\mathbf{p}}$ with respect to the data. The best model among a set of considered
 249 models is then the one that minimizes the AICc, i.e the one that has both a high goodness of fit (high
 250 likelihood) and a limited complexity (limited number of parameters).

251 In practice, the easiest way to compare the relevance of models based on their AICc is via the
 252 Evidence Ratio (ER) (Burnham & Anderson, 2010, para. 2.10). This is defined such that, for any
 253 model $M_{Z,i}$ among N_m models,

254
$$ER_i = \exp \left(\frac{1}{2} \left[AICc_i - \underbrace{\min_{j=1,\dots,N_m} (AICc_j)}_{\text{best a priori model}} \right] \right)$$

255 The ER is therefore 1 for the best *a priori* model and grows exponentially as the models become less
 256 and less adapted. From expert knowledge an ER of 2 for a given model does not justify giving

257 preference to the best a priori model over it, whereas an ER of 18 clearly favors the best a priori
258 model (Burnham & Anderson, 2010, para. 2.10).

259 2.2.4. SCAP1D: a robust estimation procedure

260 The methods presented are supposed to get an adequate RF model to avoid estimates errors: without
261 modeling precaution, they are only valid under the condition that the data can be described by an SSO
262 and ergodic RF. However, since classical regression techniques coupled with generic autocorrelation
263 models can easily approximate autocorrelograms and covariograms, the estimates of RF model
264 parameters are generally carried out by LSE on raw data without prior verification of these two
265 hypotheses (O'Connor & Kenshel, 2013; Ravahatra et al., 2017; Schoefs et al., 2016). Such a
266 procedure can then lead to important errors, in particular on the estimation of the scale parameter α ,
267 and in particular in the cases of non-stationarity in the mean and/or of important measurement noise
268 (Clerc et al., 2019)

269 To prevent these errors, we use here the SCAP-1D procedure² (Clerc et al., 2019). Based on
270 previously presented tools, it allows, from a single trajectory with few measurement points, the
271 estimation of parameters of a unidimensional noisy Trend-Stationary RF with piecewise polynomial
272 mean, constant variance and constant autocorrelation model.

273 The concept behind SCAP-1D is to ensure the reliability of the parameters' estimates by testing and
274 validating the following hypotheses:

- 275 • *H1*: validity of the RF mean model and its parameter estimates; i.e. Second-Order Stationarity of
276 centered RF;
- 277 • *H2*: validity of both the joint pdf and autocorrelation function models of the RF and of the
278 estimation of their parameters; i.e., normality of the standard source GRF, obtained by
279 isoprobabilistic transformation of the RF from estimates considering the *a priori* model;

² Spatial Correlation Assessment Procedure for Unidimensional Data

280 • *H3*: ergodicity of the trajectory; i.e., non-correlation of the data at infinity or determination of all
281 geostatistical parameters from this trajectory.

282 The SCAP-1D flowchart is shown in Figure 3. It is organized into four successive steps, which may
283 be repeated when the estimates do not validate hypotheses on the RF model:

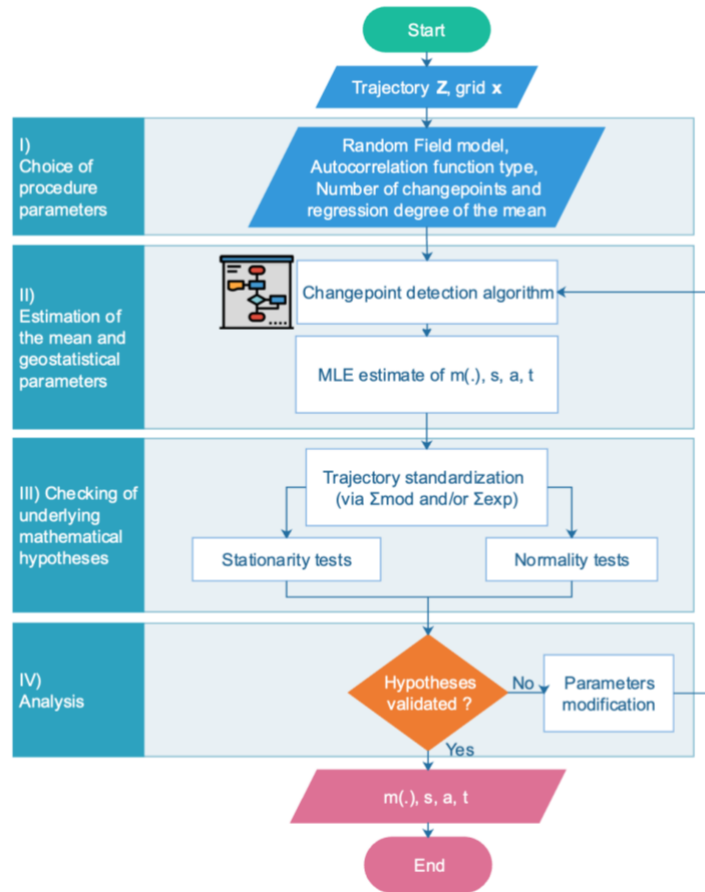
284 • *Step I) Choice of SCAP-1D parameters*, namely piecewise polynomial mean model (regression
285 degree, number of changepoints), RF joint pdf and autocorrelation function. We recommend to
286 plot the trajectory, its histogram and its experimental semivariogram to facilitate it.

287 • *Step II) Estimation of the mean and geostatistical parameters*: changepoints in the mean and their
288 significance are determined using PELT (Pruned Exact Linear Time) optimal partitioning
289 algorithm of (Killick et al., 2012). Estimation of RF parameters is then performed by the approach
290 presented in 2.2.2³.

291 • *Step III) Checking of underlying mathematical hypotheses*: plausibility of estimated model is
292 checked by checking ergodicity and performing stationarity tests (DF-test (Dickey & Fuller,
293 1981), KPSS-test (Kwiatkowski et al., 1992)) and normality tests (χ^2 , KS-test (Kolmogorov-
294 Smirnov)) on standardized trajectory, based on Step II estimates.

295 • *Step IV) Analysis*: based on Step III tests, model chosen in Step I and estimates made in Step II
296 are either accepted (algorithm ends) or rejected (modification on Step I parameters is required).

³ or by wLSE on the experimental semi-variogram in the case of non-explicit density models.



297

298

Figure 3 - General flowchart of SCAP-1D

299

In Step III, standardization of the trajectory is done by Cholesky transformation considering either:

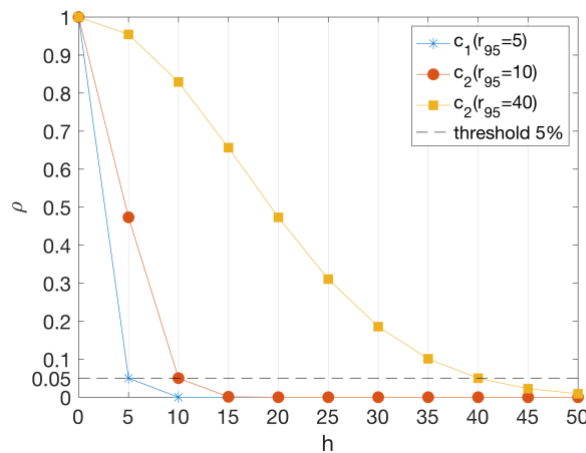
- 300 • the empirical covariance matrix: in that case, we only test H1 as tests results only depend on data
301 and estimates of the mean. Tests are then called Σ_{exp} -tests;
- 302 • or the modeled covariance matrix: in that case, we test H1 to H3 together as tests results depend
303 on the whole estimates. Tests are then called Σ_{mod} -tests.

304 2.2.5. Interpretability criterion

305 In step IV of SCAP-1D, estimates must be analyzed for their physical consistency. In particular, an
306 interpretability criterion can be defined for the estimated practical range. The point is to ensure, with
307 respect to the spacing Δx between measurements, that the variability thus described is indeed a spatial
308 variability and not a local or point variability. This is illustrated in Figure 4, where the Gaussian
309 autocorrelogram is plotted on a measurement grid of step $\Delta x = 5$ for three practical range values
310 ($r_{95} < 2\Delta x$, $r_{95} \approx \Delta x$, and $r_{95} > 2\Delta x$):

- 311 • when $r_{95} \geq 2\Delta x$ (curves c3 and c2): the variability described is spatial variability since there is
312 at least one significant intermediate spatial correlation value between a point's total correlation
313 with itself and the minimal 5% correlation associated with the practical range;
- 314 • when $r_{95} < 2\Delta x$ (curve c1): the variability described may be local or point variability since there
315 is no significant intermediate spatial correlation value to account for spatial variability.

316 Therefore, care will also be taken to ensure that the criterion $r_{95} \geq 2\Delta x$ is met when applying SCAP-
317 1D⁴.



318

319 *Figure 4 - Interpretability of practical range, measurement step $\Delta x = 5$*

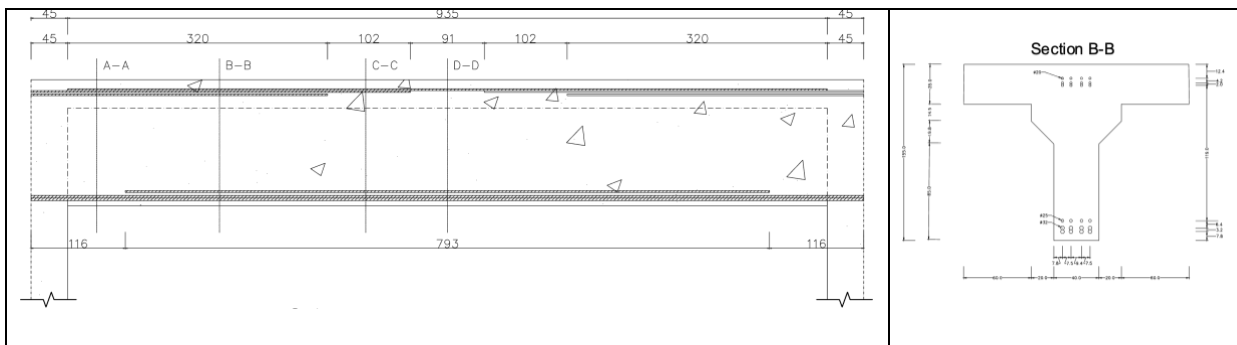
320 **3. Presentation of the structure and the measurements**

321 **3.1. Presentation of the wharf, the beam and its material**

322 The reinforced concrete beam inspected in the framework of the APOS research operation is a T
323 hyperstatic beam named "J beam" whose dimensions and reinforcement are presented in Figure 5. It
324 is located on lane 51 of the gangway 5 of the coal terminal of Montoir-de-Bretagne (Loire-Atlantique
325 department, France) with GPS coordinates: 47.32°N, -2.17°E. This terminal, built between 1981 and
326 1983 on the banks of the Loire and less than 7km from the Atlantic Ocean, is 234.4m long and 20.7m

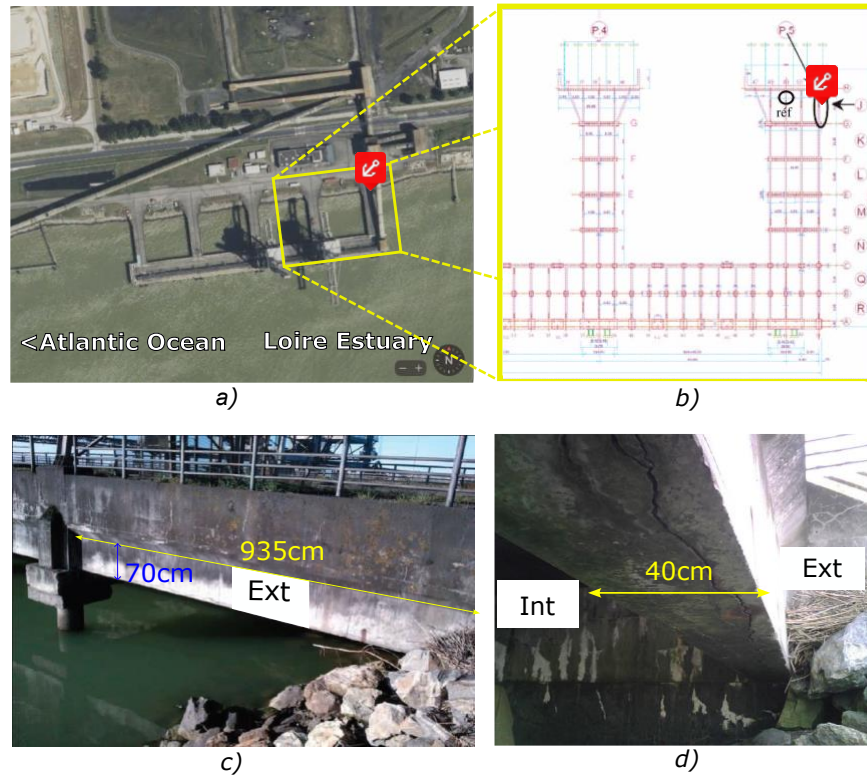
⁴ This criterion is constructed similarly to that of (Der Kiureghian & Ke, 1987) on the ability of a discretization grid to render the spatial variability properties of a RF.

327 wide and is located at +8.40m NGF (Figure 6). This proximity to the ocean implies the existence of
 328 a tidal phenomenon with an amplitude of 5.80m and a salinity of the water equivalent to maritime
 329 conditions at high tide (about 30g Cl/L). Thus, at the highest tidal coefficients, the lower face of
 330 beam J, located 5.80m above the Loire level, is in contact with the water about 2 days per month.
 331 Finally, one of the particularities of the J-beam is its location on the edge of the quay. It has a side
 332 exposed to the wetting-drying cycles, noted Ext, and a sheltered side, noted Int (see Figure 6).



333 *Figure 5 - Size and position of rebars of the "J-beam"*

334 Data from the construction archives indicate that the concrete used to build the structure is a Portland
 335 cement concrete CEMI 42.5N dosed at 350kg/m³. The mass fraction of m_{cl} clinker is thus higher
 336 than 90% and that of secondary constituents such as gypsum does not exceed 5%. The aggregates
 337 used are sand 0/6, and gravel 5/10 and 10/25. Concrete water porosity ε , measured on the central part
 338 of 5 specimens used for chloride titration was 13.7% in average and minimum and maximum values
 339 were 11.3% and 15.9% respectively. The average compressive strength f_{cm} , measured on 4 specimens
 340 of 5 cm diameter and 10 cm length was 43.5MPa, with minimum and maximum values of 38.5 MPa
 341 and 48.9 MPa, respectively.



342

343

344

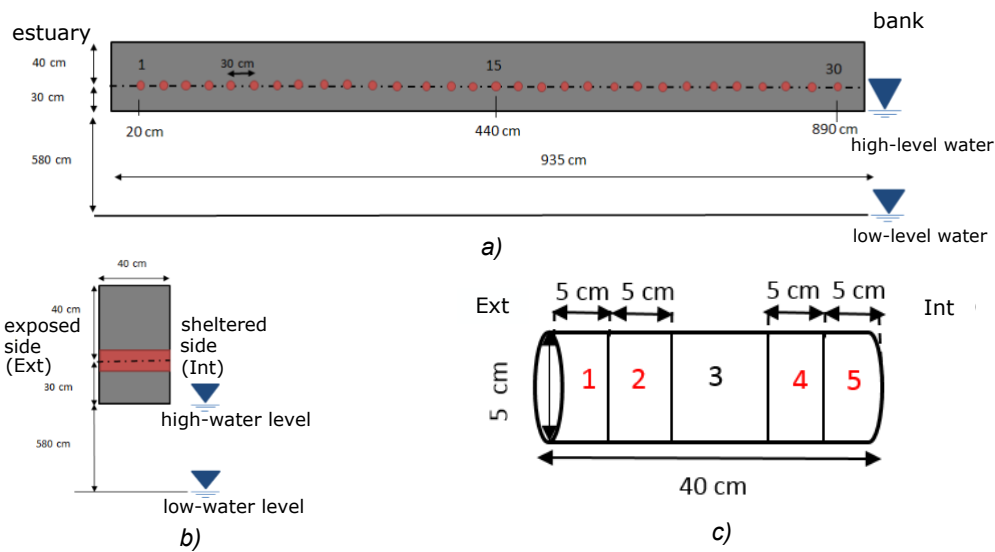
Figure 6 - Different views: a) Aerial view, b) Sketch of bridge 3, 4 and 5, c) Beam J, d) Exposed (Ext) and sheltered (Int) side of beam J.

345 3.2. Total chloride content measurements at 28 years

346 3.2.1. Available data set

347 Chloride content measurements were performed on 30 through cylindrical cores extracted on the J-
 348 beam at the same height of 30 cm and with lateral spacing of 30 cm (see Figure 7) (Othmen et al.,
 349 2018). Extraction was carried out in 2011-2012, after 28 years of exposure. From initial dimensions
 350 of 5 cm in diameter and 40 cm in length, each core was divided into 5 slices (identified on Figure 7).
 351 Slices 1, 2, 4 and 5 were used to determine the chloride profiles, using the procedure recommended
 352 by the RILEM TC 178-TMC (Vennesland et al., 2013). Slices 1 and 2 are associated to the exterior
 353 side (gathered in Ext specimens) and slices 4 and 5 to the interior side (gathered in Int specimens).
 354 Whereas deep slices 2 and 4 were 40-mm thick with measures in 10 mm increments, slices 1 and 2
 355 were 45mm-thick with measures in 5-mm increments to catch the value at the surface. Slice 3 was
 356 used for further investigation such as porosity, compressive strength and estimation of the initial
 357 chloride content. Out of a total of 30 specimens per side, 16 were usable on the Ext Face (53%), and

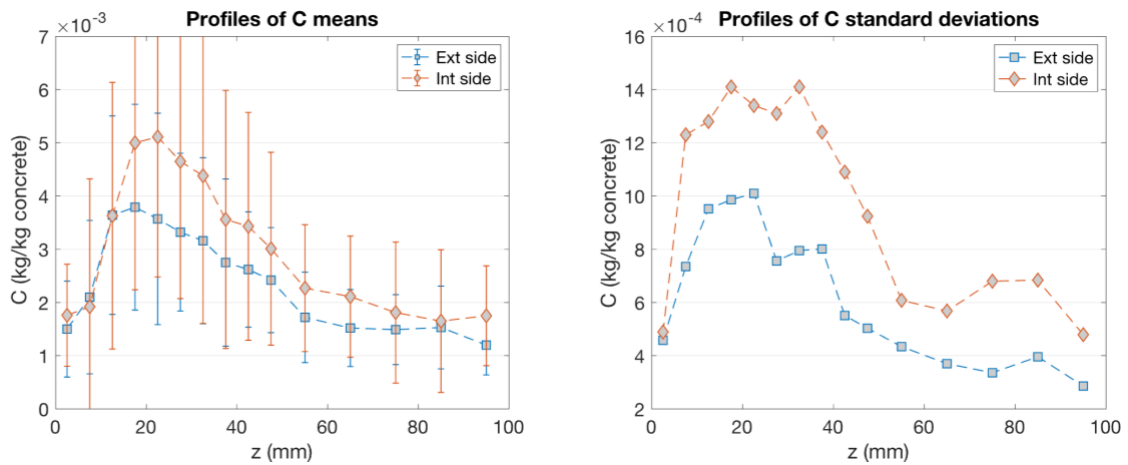
358 21 on the Int Face (70%). Moreover, out of the 555 total chloride content from the 30 specimens thus
 359 considered, only 460 were usable (83%, i.e., 51% of all the measurements initially planned).



360

361 *Figure 7 - Samples taken for chloride titration (J-beam): a) Locations, b) Cross-section, c) Slices*

362 Figure 9 hereafter represents then the set of remaining measurements of total chloride content at 28
 363 years finally considered (noted C in the following). Evolutions of empirical mean and standard
 364 deviation by depth and by face are represented on Figure 8.



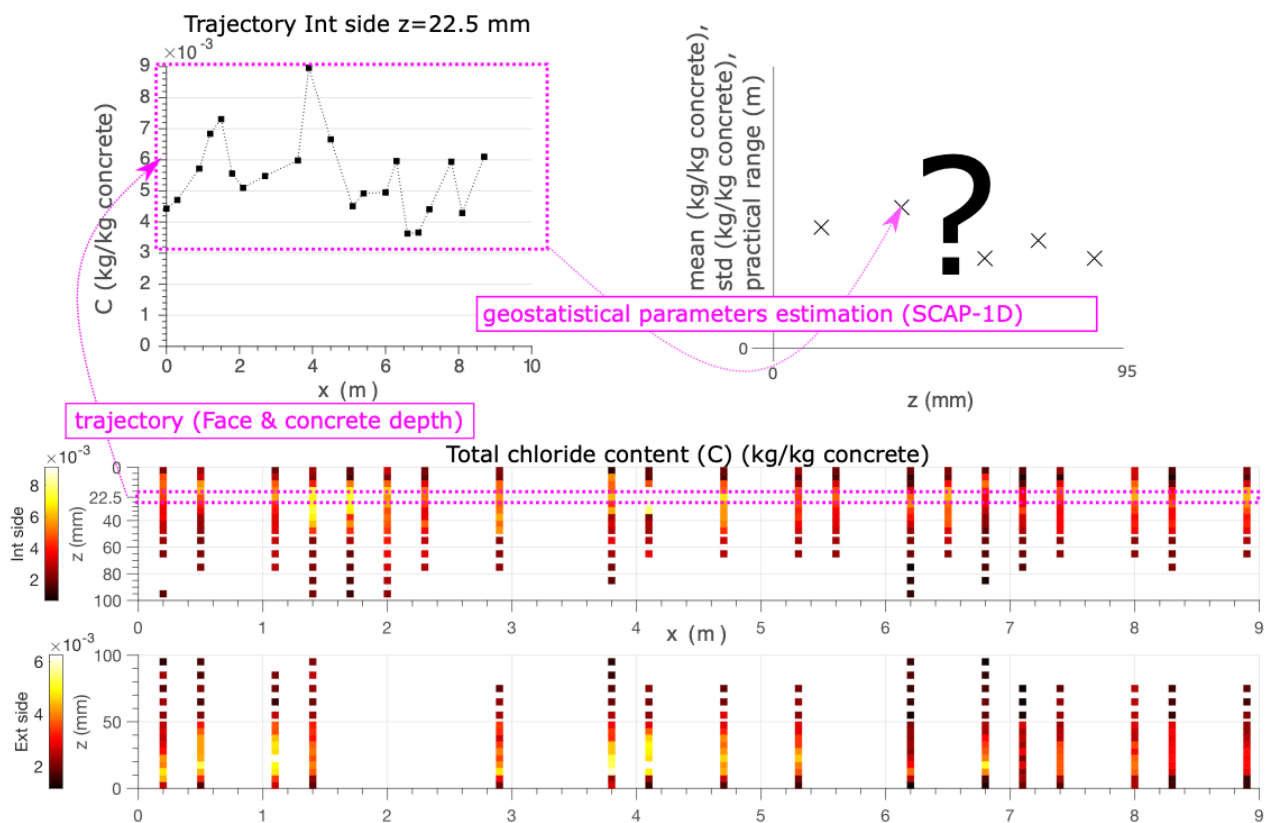
365

366 *Figure 8- Profiles of the evolution of the statistical mean and standard deviation of total chloride*
 367 *concentrations according to the depth of embedding*

368

369 3.2.2. Constitution of trajectories

370 In the following, the evolution of the SV of C is analyzed as a function of depth and exposure
 371 conditions. SCAP-1D is then applied to horizontal trajectories of measurements performed on the
 372 same face and at the same embedding depth z . The estimation of geostatistical parameters for each
 373 trajectory allows then plotting their evolution as a function of z and exposure face. This study
 374 principle is illustrated in Figure 9.



375
 376 Figure 9 - Total chloride concentration database and illustration of the principle of implementing SCAP-1D
 377 on total chloride concentration data

378 3.3. Average diffusion parameters at 28 years

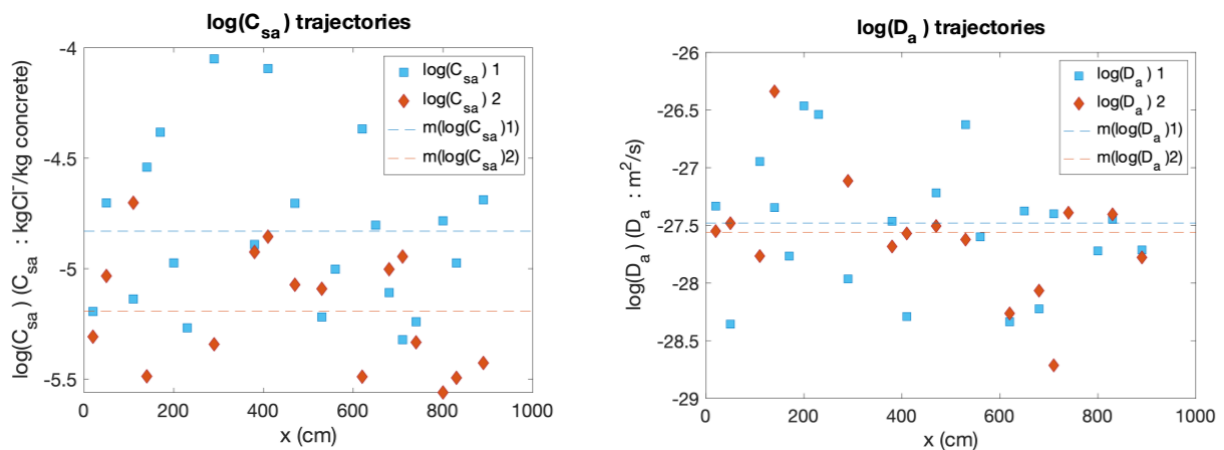
379 The 37 total chloride profiles were post-processed for determining associated Fick's second law
 380 average diffusion parameters at reference time t_r of 28 years, noted C_{sa} and D_a . The fitting procedure
 381 to the peak of the profiles is described by (Othmen et al., 2018) and implemented in Schoefs et al.
 382 (2023). Thus, a trajectory for each diffusion parameter per side, located at a height of 30 cm, is built.
 383 These include 16 points for the Ext Side and 21 points for the Int Side, with a minimum spacing of
 384 30 cm between measurement points. Table 2 summarizes this information and Figure 10 shows

385 trajectories. Note that log function is applied to each parameter for (i) simplifying the representation
 386 and visual analysis because they are assumed to be lognormally distributed, (ii) using procedures of
 387 identification (see section 4.2) available for normally distributed random fields.

388 *Table 2- Numbering of the trajectories of average scattering parameters (J-beam)*

trajectory	Side	number of measurement points
$\log(C_{sa})$ 1	Int	21
$\log(D_a)$ 1	Int	21
$\log(C_{sa})$ 1	Ext	16
$\log(D_a)$ 2	Ext	16

389



(a) Trajectories and statistical means of logarithms of the 28-year average surface concentrations of total chlorides - beam J

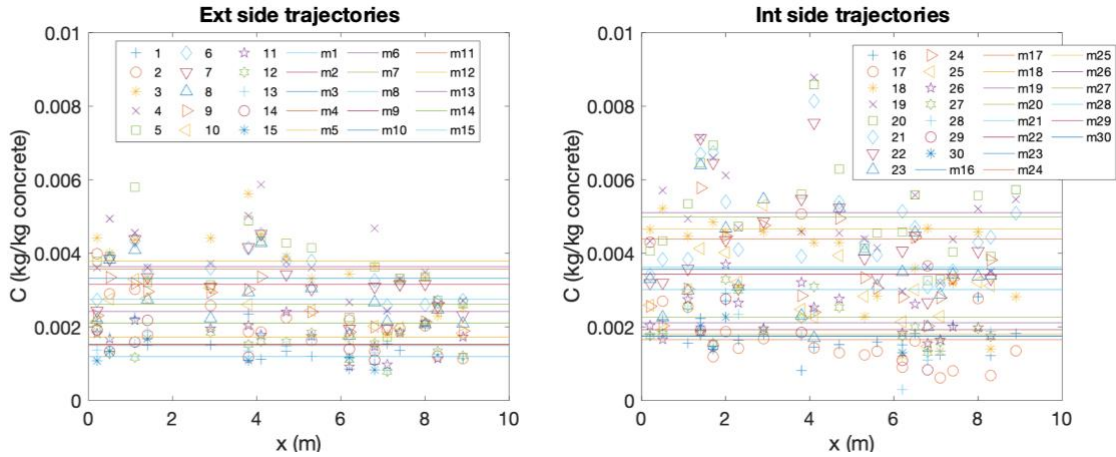
(b) trajectories and statistical means of the logarithms of the mean diffusivities of total chlorides at 28 years - beam J

390 *Figure 10 - Trajectories and statistical averages of the logarithms of the mean diffusion parameters at 28*
 391 *years (J-beam)*

392 4. Spatial variability estimates of total chloride content in J-beam and physical 393 understanding

394 4.1. Preamble: trajectories conditioning (kriging, debiasing)

395 Taking into account the non-usable or missing measurements per specimen and in order to consider
 396 the maximum number of points per trajectory, these are first enriched by ordinary kriging of the
 397 available data (Baillargeon, 2005, Chapter 4; Chilès & Delfiner, 2012, Chapter 3). The preliminary
 398 plot of raw trajectories does not reveal any apparent non-stationarity (Figure 11) and the expectation
 399 of their associated RF is not known.

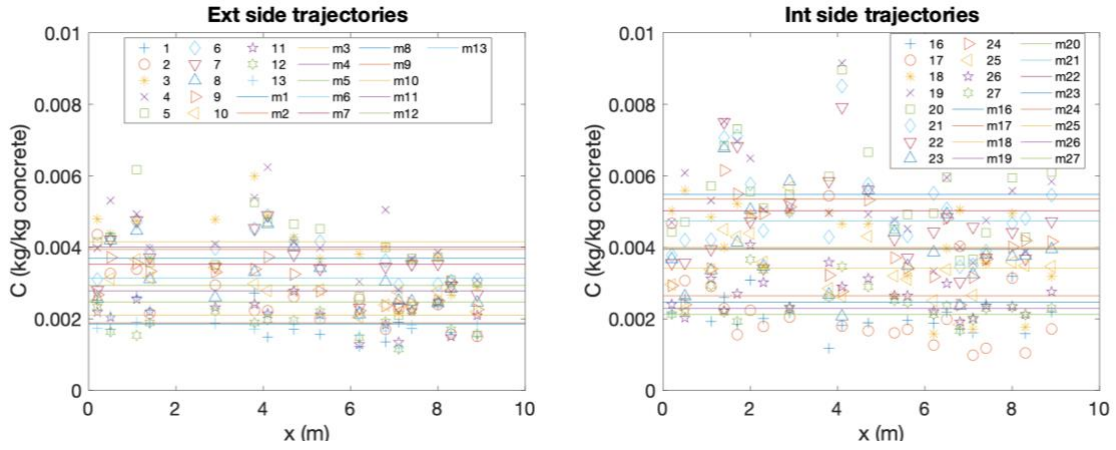


400

401 *Figure 11 - Raw trajectories and associated statistical means - trajectory number / depth correspondences*
 402 *presented in Table 5*

403 The kriging is then performed from the identification by weighted Least-Square Estimate (wLSE) of
 404 the semi-variograms of the initial trajectories. We consider an exponential covariance model and the
 405 existence of an additive measurement error, identified by (Bonnet et al., 2017). Moreover, (Bonnet et
 406 al., 2017) also identified a measurement bias $b = 0.37 \times 10^{-3}$ (kg/kg concrete) associated with the
 407 measurement protocol used and with human errors during its implementation. All the measurements
 408 are therefore debiased before kriging so that the data considered are now $C + b$. In order to limit the
 409 influence of the kriged data on the estimation of the SV of C , only the trajectories for which their
 410 proportion is lower than 25% are considered.

411 A total of 13 trajectories of 16 points can be considered on the Ext side ($z \in [2.5; 75]$ mm) and 12
 412 trajectories of 21 points on the Int side ($z \in [2.5; 65]$ mm). The number of kriged data per trajectory
 413 is detailed in Table 5 in Appendix, and the selected debiased trajectories are shown in Figure 12. Less
 414 than 25% data are kriged until 65-mm depth for both sides. We point out that due to the absence of
 415 measurements at the abscissae of the non-exploitable specimens, the trajectory grids are irregular,
 416 with 30% of measurements missing for the Int side and 53% for the Ext side. The performances of
 417 the SCAP-1D normality tests are therefore affected (Clerc et al., 2019) and particular care must be
 418 taken to ensure the consistency of the estimation results.



419

420

Figure 12 - Selected trajectories and associated statistical means

421 **4.2. Geostatistical pre-study and choice of parameters (Step I):**

422 We recall that the trajectories studied are debiased. We then denote \tilde{Z} the RF of C such that

$$\tilde{Z} = Z - b \quad | \quad b = -0.37 \times 10^{-3} \text{ kg/kg concrete} \quad (4)$$

423 Moreover, (Othmen et al., 2018) have previously determined that the marginal law of C is lognormal
 424 and (Bonnet et al., 2017) have identified the "measurement error" introduced by the measurement
 425 protocol, but for a mortar only. This is distributed according to a generalized extremum law
 426 (GeV, (Johnson et al., 1995, p. 3)) with parameters $k = 0.16$, $\sigma = 9.3 \times 10^{-5}$ and $\mu =$
 427 -8.4×10^{-5} . Schoefs et al. (2023) have recently highlighted that the model of error varies
 428 according to the chloride content. As a consequence, the error should vary according to each
 429 trajectory. For simplicity, it is considered as constant in the paper and its standard deviation is
 430 an average of the potential standard deviations (Schoefs et al., 2023).

431 The best fitting RF model for \tilde{Z} is then the sum of a log-normal RF Y and a GeV random variable
 432 (r.v) W so that, following Equation (1), $Z = Y + W$.

433 However, the joint pdf of such a RF is not explicit and SCAP-1D cannot then be simply applied.
 434 The small number of points per trajectory also excludes an estimation by wLSE on semi-variograms
 435 (see 2.2.2).

436 Two modeling compromises are then possible in order to guarantee explicitness:

437 • Model a: consider a normal marginal distribution of total chloride content and a normal
 438 distribution of the error, so that

$$\tilde{Z} \sim \underbrace{N(\mu(x), s. R(a))}_{G^1} + t. N(0, I) \quad (5)$$

439 where s and t are respectively the empirical variance of the signal and the error and $R(a)$ is the
 440 autocorrelation matrix.

441 • Model b: do not consider the measurement error, whose standard deviation (1.55×10^{-4} kg/kg
 442 concrete according to the model of (Bonnet et al., 2017)) would induce a maximum CoV of 8.3%
 443 (on trajectory 13; Ext side, $z = 75$ mm). For this model,

$$\tilde{Z} \sim \exp\left(\underbrace{N(\mu(x), s. R(a))}_{G^2}\right)^{LN} \quad (6)$$

444 G^1 and LN are then the RF describing the SV of C , with G^2 the source GRF of LN .

445 The first approximation of the maximum CoV according to the model of (Bonnet et al., 2017) being
 446 significant, we subsequently apply SCAP-1D considering both models so that :

- 447 • if the Signal-to-Noise Ratio (SNR) associated with model a is low, the error is non-negligible and
 448 model a is retained;
- 449 • if the SNR associated with model a is high, the error is considered negligible and model b is
 450 retained.

451 Because of the absence of non-stationarities visible in Figure 12, the trajectories are *a priori* assumed
 452 to be stationary, so that $\mu(x) = \mu$. We also recall that the autocorrelation function model chosen for
 453 G^1 and LN is exponential. According to (Chilès & Delfiner, 2012, p. 106), to guarantee such a
 454 model for the autocorrelation function $\rho_{LN}(a)$ of LN , the autocorrelation function ρ_{G^2} of G^2 must
 455 be written

$$\rho_{G^2}(\cdot) = \ln(\rho_{LN}(\cdot) \cdot [e - 1] + 1) \quad (7)$$

456 Still according to (Chilès & Delfiner, 2012, p. 106), the mean m_{LN} and the variance σ_{LN}^2 of LN
 457 are then written

$$m_{LN} = \exp\left(\mu + \frac{1}{2}s\right) \quad (8); \quad \sigma_{LN}^2 = m_{LN}^2(\exp(s) - 1) \quad (9)$$

458 **4.3. Model a: Parameter estimation, hypothesis testing and analysis (Steps II, III**
 459 **and IV)**

460 *Preliminary note: Before estimation, the trajectory data, of order 10^{-3} , are multiplied by a factor*
 461 *$k = 10^4$ to facilitate the convergence of the MLE. The estimates of t , s and μ are then transformed*
 462 *accordingly before analysis.*

463 Table 6 in Appendix details the results of the SCAP-1D implementation considering model *a*. Only
 464 the results of the Σ_{mod} -tests are considered due to the small number of points per trajectory.

465 Analyzing these, the estimates for trajectories 4 and 5 are rejected due to the rejection of the
 466 stationarity hypothesis by the KPSS-test and because the estimated error and practical range are
 467 zero and well below $2\Delta_x$, respectively, so that the spatial correlation of the data cannot be described
 468 (see 2.2.5). This is also the case for trajectories 2, 11, 12, and 13 and can be explained by their very
 469 small numbers of points. Similarly, the estimates associated with trajectories 15, 17 and 24 are not
 470 considered because the estimated practical range is zero. Finally, no valid and convergent estimate
 471 can be obtained for trajectory 14. As a first step, we plot for each selected trajectory the estimates
 472 $\hat{\mu}$ of the mean with their 95% MLE-based confidence intervals in Figure 13 (a)⁵, and the estimates
 473 $\sqrt{\hat{s} + \hat{t}}$ of the standard deviation in Figure 13 (b), for which the distribution is unknown. We then
 474 note that these are consistent with the statistical mean and standard deviation profiles previously
 475 plotted in Figure 8: the estimated values through kriging (see 4.1) do not create disturbance of these
 476 statistical estimates.

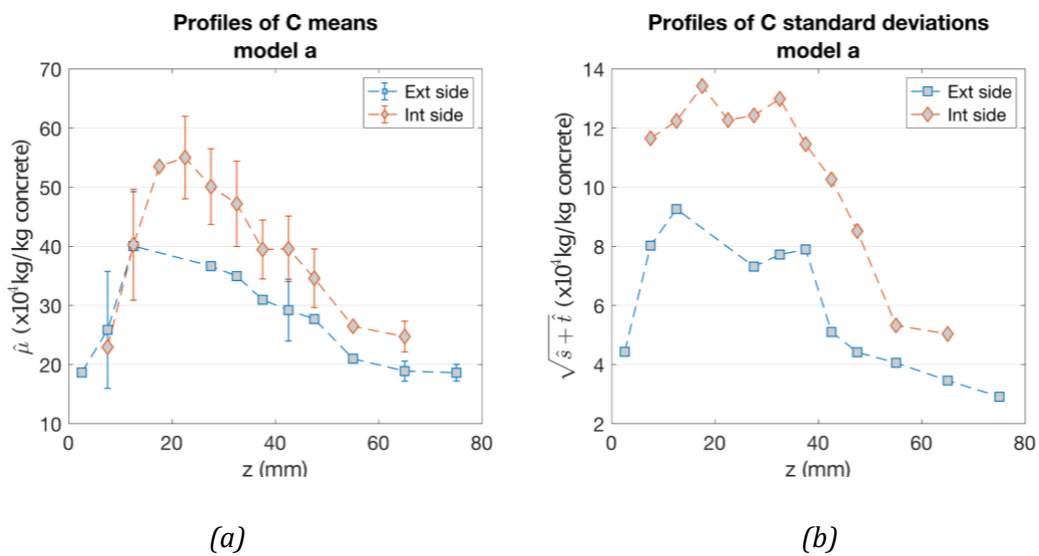
477 As a second step, we plot in Figure 14 (a) the standard deviation estimates $\hat{\tau} = \sqrt{\hat{t}}$ and $\hat{\sigma} = \sqrt{\hat{s}}$ of
 478 the error and the signal respectively as well as the standard deviation τ_ε associated with the error
 479 model of (Bonnet et al., 2017). Trajectories for which the estimated error is zero are not considered.

⁵ some values are missing due to the singularity of the Fisher matrix

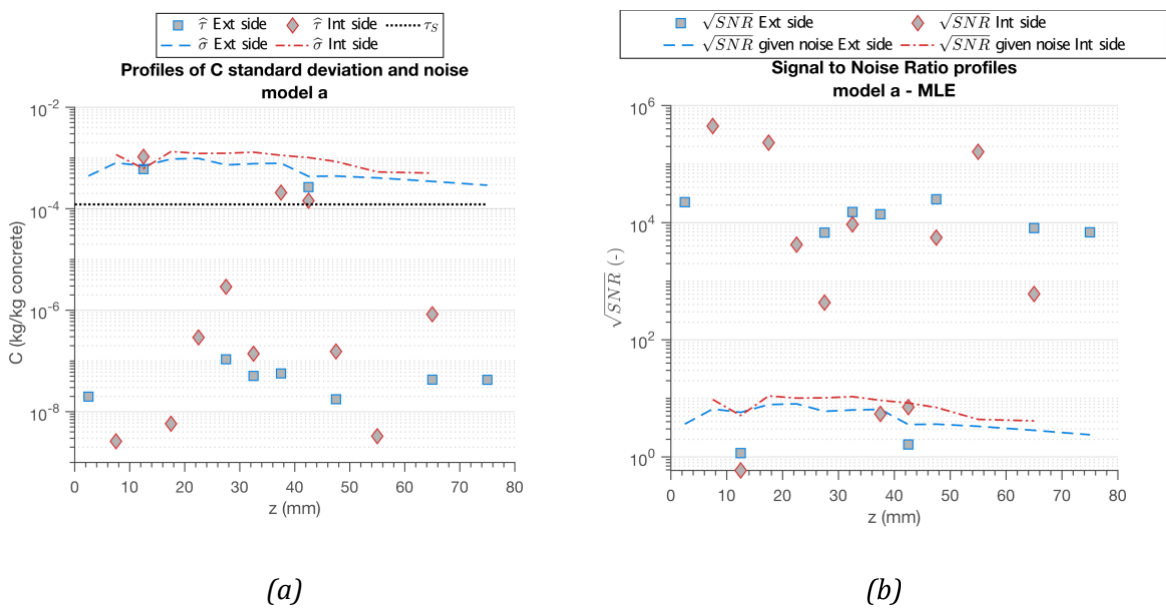
480 We then compare in Figure 14 (b) the roots of the experimental SNRs \hat{t}/\hat{s} and the fixed error SNRs
 481 $\tau_\varepsilon^2/\hat{s}$. Thus, we note that 75% of the roots of the experimental SNRs are greater than 100 and with
 482 no specific trend of evolution along z . The fixed error SNRs are logically lower than the
 483 experimental ones because the error was computed for mortars for which the error of assessment
 484 is larger (Schoefs et al., 2023).

485 In accordance with the previously stated modeling assumptions, we therefore consider the
 486 measurement error negligible and retain model b for the SCAP-1D trajectory study.

487



488 *Figure 13 - Profiles of the evolution of the mean and standard deviation of total chloride content according*
 489 *to the depth - model a*



490
491

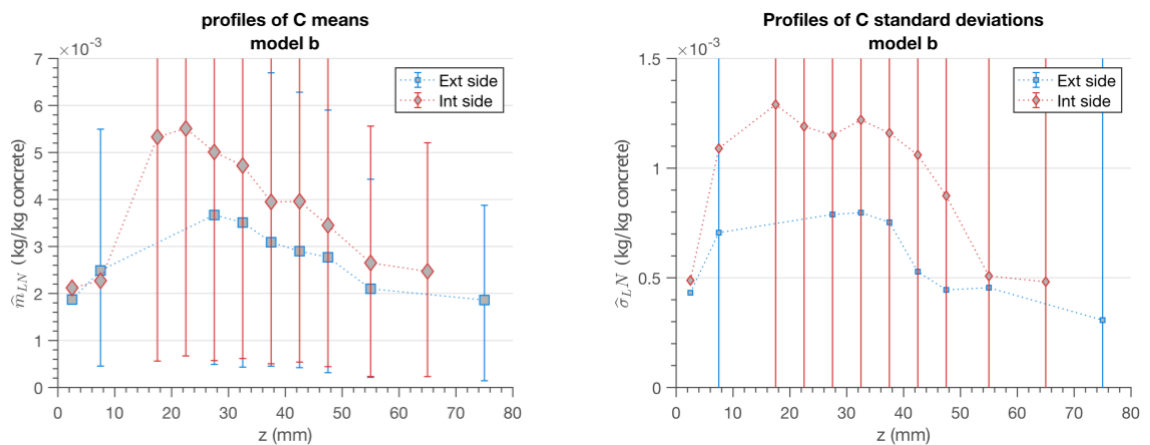
Figure 14 - Study of the Signal to Noise Ratio - model a

492 **4.4. Model b: Parameter estimation, hypothesis testing and analysis (Steps II, III, IV)**

493 Preliminary note: Since the RF considered in model b is log-normal, the data considered for the
494 SCAP-1D implementation are the logarithms of the debiased data to consider a normal joint pdf. The
495 estimators of m_{LN} , σ_{LN}^2 and $r_{95,LN}$ are then calculated from Equations (7) to (9) and from the
496 estimators \hat{s} , \hat{t} and \hat{a} .

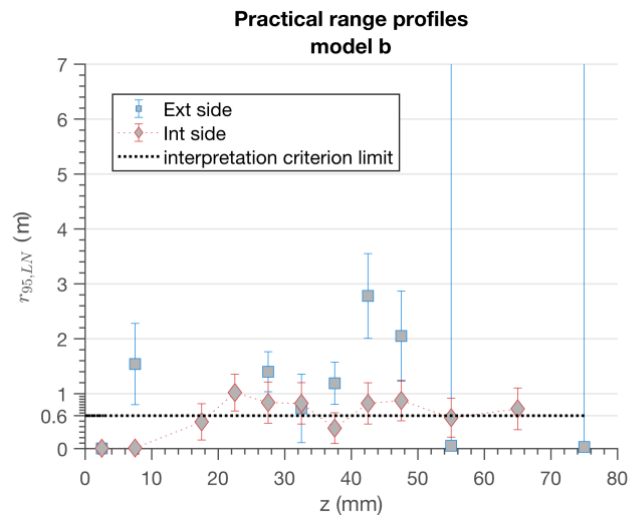
497 Table 7 in Appendix shows the result of the SCAP-1D implementation considering model b. Only
498 the results of the Σ_{mod} -tests are considered due to the small number of points per trajectory. Analyzing
499 these, the estimates for trajectories 3, 4, 5 and 16 are rejected due to the rejection of the stationarity
500 hypothesis by the KPSS-test. A model of the mean and covariance function that satisfies the
501 hypothesis cannot be found, so no geostatistical parameter estimates are available for these
502 trajectories. 77% of the estimates are then valid on Ext side (10/13) and 92% on Int side (11/12).

503 The estimates \hat{m}_{LN} and $\hat{\sigma}_{LN}$ of the means and standard deviations are plotted with their confidence
504 intervals (CIs) for each trajectory in Figure 15. Note that the estimates are consistent with the
505 statistical mean and standard deviation profiles previously plotted in Figure 8. The estimates $\hat{r}_{95,LN}$
506 of the practical ranges, meanwhile, are plotted with their CIs in Figure 16.



507 Figure 15 - Profiles of the evolution of the mean and standard deviation of total chloride concentrations
508 according to the depth of embedding - model b

509



510

511 *Figure 16 - Practical range profiles of total chloride concentration trajectories as a function of embedment*
 512 *depth - model b*

513 In the case of the trajectories associated with the Ext side, only 8 out of 10 estimates retained by
 514 SCAP-1D (i.e., 47% of all estimates) are finally retained after filtering out the outliers. These
 515 estimates all meet the interpretability criterion (see 2.2.5) with values between 1 and 3 m for a
 516 minimum measurement step of 30 cm. Contrary to the assumptions made at the beginning of the
 517 study, however, there is no trend in the evolution of $\hat{r}_{95, LN}$ as a function of the depth.

518 In the case of the trajectories associated with the Int side, all the estimates retained by SCAP-1D can
 519 be considered after filtering out the outliers (i.e., 92% of all the estimates). In accordance with the
 520 hypotheses formulated at the beginning of the study, we observe a zero practical range near the
 521 surface, then a quasi-constant value around 60 cm-1 m from 20 mm depth, respecting the
 522 interpretability criterion. This tendency reflects a transition from a purely random quantity of interest
 523 (q.i) at the surface to a spatially correlated q.i. at depth. We propose following explanation:

- 524 • At the surface, many spatio-temporally random material (micro-cracks, ...), physico-chemical
 525 (local runoff, ...), and environmental phenomena (biofouling, ...) contribute to the supply and
 526 convection of chlorides so that, in coherence with the central limit theorem, the concentration of
 527 chlorides at the surface can be considered totally random, at least at the scale of the 30 cm spatial
 528 discretization studied;

529 • at depth, the phenomenon of diffusion and fixation of C gradually takes precedence over their
530 distribution within the coating, so that the fixation and diffusion properties of the concrete become
531 predominant compared to the external and surface phenomena. Since the concrete has a certain
532 spatial homogeneity, it is then consistent that C is spatially correlated.

533 Furthermore, it is noted that the value of $\hat{r}_{95, LN}$ at the rebar depth is of the same order as the as the
534 conventional spacing of the vibrations during concrete pouring, from 30 to 60 cm (Guiraud, 2018;
535 SETRA, 2005, p. 199). This remark then reinforces the idea that the spatial correlation of C is strongly
536 related to the homogeneity properties of concrete.

537 ***4.5. Model b: construction of a unique autocorrelation model of chloride content***

538 The results obtained from the study of the Int side trajectories are much more convincing than those
539 from the study of the Ext side ones. In order to propose a unique autocorrelation model of C for the
540 diffusion region, we then perform an MLE on the set of reduced centered trajectories of the Int side
541 (without the first 10 mm), considering a unique scaling parameter a . Because of the non-stationarity
542 in mean and variance of C according to depth, we consider the trajectories independent of each other
543 (we therefore neglect SV along z -axis). Still considering an exponential covariance model, the
544 estimated practical range is $\hat{r}_{95} = 0.71$ m, i.e, $\hat{a} = 0.24$ m.

545 We then state that the Gaussian model of identical practical range has the scale parameter $\hat{a} = 0.41$
546 m. The calculation of the ER from the AICc however, does not allow distinguishing between the two
547 models from the data, either by considering each trajectory or from the MLE estimate over all
548 trajectories. Indeed, their values lie between 1 and 1.29. These are reported in Table 8 in Appendix.

549 By considering only the estimation results from the Int side, which are considered more robust due to
550 the larger amount of data per trajectory, we can partially answer the questions raised in the
551 introduction of this study. The SV of chloride content indeed seems to depend on the depth, with a
552 large variability within the convection zone, and much less and more stable in the diffusion zone with
553 a practical range of about 70cm. This value is however more than two to three times lower than

554 the practical range values of the average diffusion parameters C_{sa} and D_a reported in the
555 literature, between 1.76 and 2.64m (Engelund & Sørensen, 1998; Karimi, 2002; O'Connor &
556 Kenshel, 2013). However, we recall that the latter are obtained with less robust methods than SCAP-
557 1D and with even smaller measurement sets.

558 The question of the influence of exposure conditions on the SV of chloride content remains open,
559 however, because of the inconsistency of the practical range estimates on the Ext side. Given the
560 interpretation of the results for the Int side, however, it can be expected that it has an influence only
561 near the surface, for which the chloride contents are already spatially decorrelated. However, this
562 proposal needs to be confirmed by studying an even richer database in order to increase the
563 robustness of the estimates.

564 **5. Spatial variability estimation of chloride diffusion parameters of J-beam and physical** 565 **analysis**

566 ***5.1. Geostatistical pre-study and choice of procedure parameters (Step I):***

567 The trajectories of $\log(C_{sa})$ and $\log(D_a)$ are shown in Figure 17 to Figure 20, as well as their
568 means and the histograms and experimental semivariograms of centered trajectories. These curves
569 are plotted for each trajectory in three cases: (i) stationary mean (no changepoint); (ii) piecewise
570 stationary mean with one changepoint determined via the PELT algorithm (Killick et al., 2012);
571 (iii) piecewise stationary average at two changepoints determined via the PELT algorithm.

572 The presence of sills on the experimental semi-variograms allows identifying the *a priori*
573 stationary centered trajectories and thus the most appropriate non-stationarity model for each.
574 The shapes of the histograms and semi-variograms (nugget effect, tangent to the origin, ...)
575 allows identifying models of joint density and a priori autocorrelation function that are adequate
576 to the geostatistical description of the data.

577 Since the amount of data per trajectory is limited, especially for the Ext side, Step I could only
 578 be executed for the trajectories $\log(C_{sa})$ 1 and $\log(D_a)$ 1. The observations made as well as the
 579 models considered *a priori* are presented in Table 3.

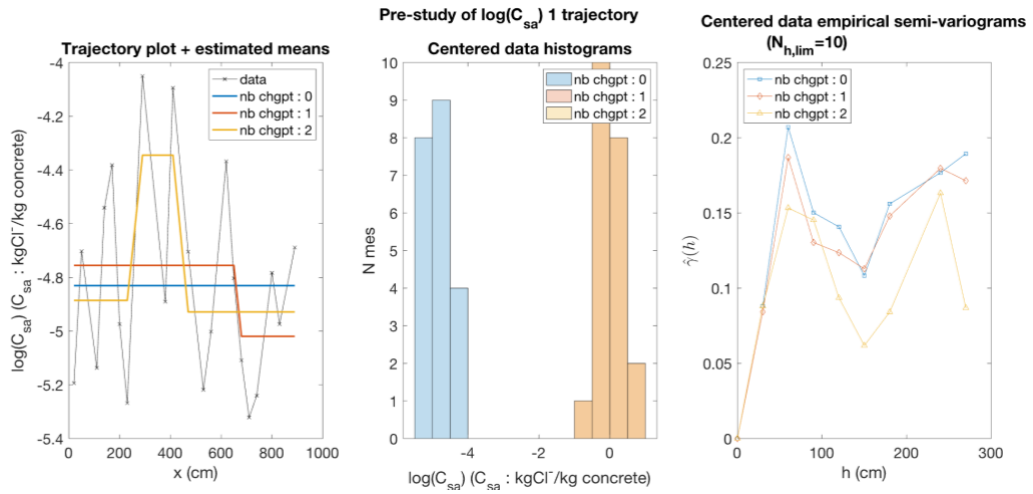
580 *Table 3- Geostatistical pre-study of the trajectories of the logarithms of the average diffusion parameters –*
 581 *J-beam*

trajectory	analysis of experimental semi-variograms and histograms					models considered		
	chgpt(*)	nugget	oscillations	original tangent	histogram shape	average	field	covariance
$\log(C_{sa})$ 1	0	no	no	insufficient resolution	asymmetrical	cste	GRF	Gauss or expon
$\log(D_a)$ 1	0	no	no	insufficient resolution	symmetrical	cste	GRF	Gauss or expon
$\log(C_{sa})$ 2	-	-	-	-	-	cste	GRF	Gauss or expon
$\log(D_a)$ 2	-	-	-	-	-	cste	GRF	Gauss or expon

(*) : changepoints necessary for the experimental semi-variogram to have a sill

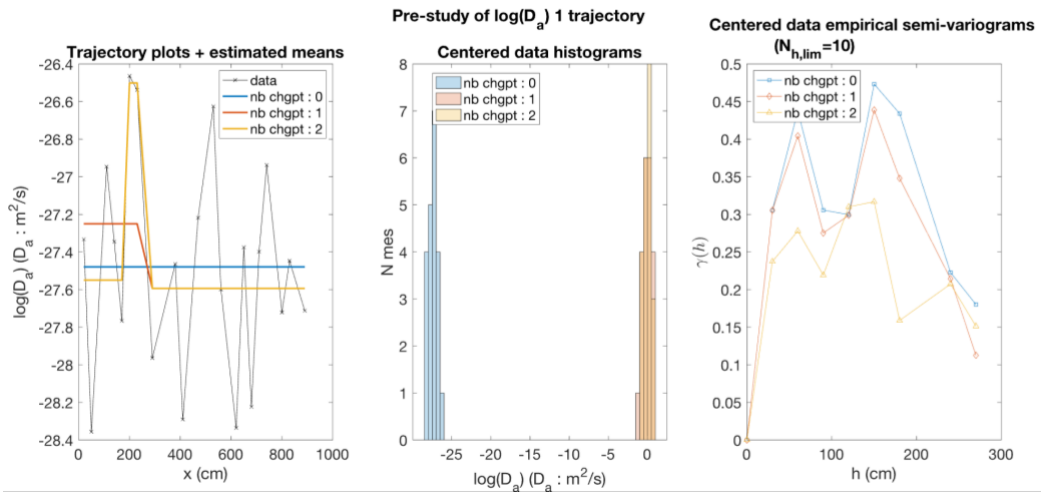
582

583



584 Figure 17- Data and averages of trajectory 1 of log mean surface concentration; histograms of trajectories so
585 centered; experimental semivariograms of trajectories so centered

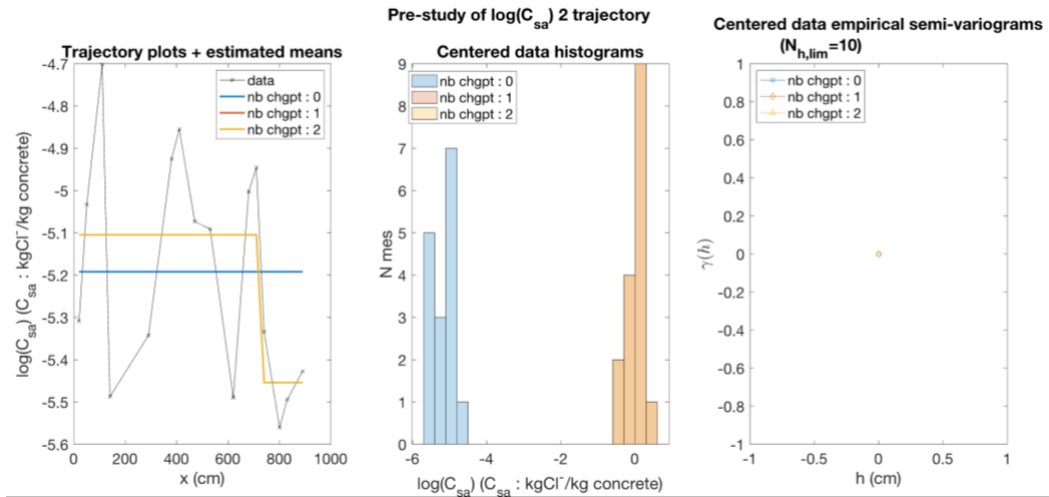
586



587 Figure 18- Data and averages of trajectory 1 of logarithm of mean diffusivity; histograms of trajectories so
588 centered; experimental semivariograms of trajectories so centered

589

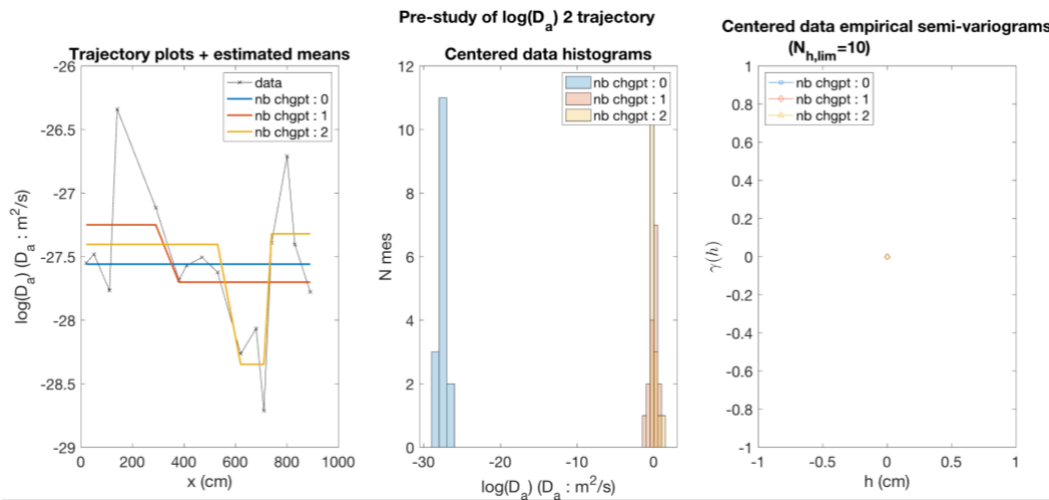
590



591
592

Figure 19- Data and averages of logarithm of mean surface concentration trajectory 2; histograms of trajectories so centered; experimental semivariograms of trajectories so centered

593



594
595

Figure 20- Data and averages of trajectory 2 of logarithm of mean diffusivity; histograms of trajectories so centered; experimental semivariograms of trajectories so centered

596 5.1.1. Fields models

597 Although the histogram of the centered trajectory $\log(C_{sa})$ 1 is asymmetric, this may be due to
 598 the spatial correlation of the data. The histogram of $\log(D_a)$ 1 is centered. Moreover, we do not
 599 notice any nugget effect. This is due to the fact that the measurement noise of the chloride data is
 600 negligible (see 4.3). For simplicity and consistency with the results of the literature, a Gaussian
 601 Random Field model (GRF) is used to estimate spatial variability. This model is also retained by
 602 default for the $\log(C_{sa})$ 2 and $\log(D_a)$ 2 trajectories.

603 *5.1.2. Averaging models: apparent non-stationarity*

604 The trajectories are *a priori* globally stationary since the experimental semi-variograms without any
 605 changepoint in the mean present a sill. A constant mean model is therefore retained.

606 *5.1.3. Covariance function models*

607 Due to the large between measurement points, the spatial resolution is insufficient to visualize the
 608 presence of a tangent at the origin of the experimental semi-variograms. We therefore retain both the
 609 Gaussian and exponential covariance models without *a priori* preference.

610 This choice does not allow accounting for the correlation between $\log(C_{sa})$ and $\log(D_a)$, well
 611 identified by (Othmen et al., 2018) and which should be modeled via a cross-correlated Random Field
 612 (XRF) (Chilès & Delfiner, 2012, p. 332). It is however justified as XRF modelling requires additional
 613 parameters (cross-correlation coefficient and cross-scale parameter(s)) which leads to
 614 overparametrization and unsuccessful assessment attempts due to the limited amount of data⁶.

615 ***5.2. Parameter estimation, hypothesis testing and analysis (Steps II, III and IV)***

616 SCAP-1D steps II and III are applied to the trajectories of $\log(D_a)$ considering the models kept in
 617 5.1. This allows the most appropriate covariance model to be determined from the calculation of
 618 Evidence Ratios (ER). These are computed from the AICc. Table 4 shows the results of SCAP-1D
 619 execution by trajectory. The models are ranked by increasing value of their ER.

620 *Table 4- Geostatistical parameter estimates of the trajectories of the logarithms of the mean scattering*
 621 *parameters by SCAP-1D*

traj	model					Σ_{exp} -tests				Σ_{mod} -tests				estimates			CoV			model selection		range	
	#	model	cov	chg	reg	χ^2	KS	KPSS	DF	χ^2	KS	KPSS	DF	$\alpha 1$	s	a1 (cm)	$\alpha 1$	s	a1	AICc	ER	r ₉₅ (cm)	r ₉₅ /L
log(C_{sa}) 1	1	GRF	expon	0	0	0	0	0	1	0	0	0	1	-4,82	0,13	17	0,02	0,31	0,81	-14,08	2,13	50	0,05
	2	GRF	gauss	0	0	0	0	0	1	0	0	0	1	-4,81	0,15	37	0,02	0,39	0,33	-15,59	1,00	63	0,07
log(C_{sa}) 2	1	GRF	expon	0	0	0	0	0	1	0	0	0	1	-5,20	0,07	19	0,01	0,36	1,20	-19,22	1,00	57	0,06
	2	GRF	gauss	0	0	0	0	0	1	0	0	0	1	-5,20	0,07	20	0,01	0,36	0,80	-19,11	1,06	35	0,04
log(D_a) 1	1	GRF	expon	0	0	0	0	0	1	0	0	0	1	-27,48	0,31	10	0,00	0,31	1,65	3,78	1,01	29	0,03
	2	GRF	gauss	0	0	0	0	0	1	0	0	0	1	-27,48	0,31	18	0,00	0,31	0,77	3,76	1,00	32	0,03
log(D_a) 2	1	GRF	expon	0	0	0	0	0	1	0	0	0	1	-27,56	0,29	13	0,01	0,35	1,40	4,19	1,00	40	0,04
	2	GRF	gauss	0	0	0	0	0	1	0	0	0	1	-27,56	0,29	19	0,01	0,35	0,72	4,21	1,01	33	0,04

⁶ MLE on raw data and MLE on data enriched via Metropolis-Hastings sampling did not give satisfactory results

622 First no estimate is rejected by the hypothesis tests. The estimates computed from the exponential
623 and Gaussian models are then consistent for each of the trajectories except for the trajectory $\log(C_{sa})$
624 2 (relative errors of respectively 21%, 63%, 9% and 21% between the practical ranges of the
625 Gaussian model and those of the exponential model). Furthermore, the exponential and Gaussian
626 covariance models cannot be distinguished from the ERs (maximum difference observed for the
627 $\log(C_{sa})$ 1 trajectory with a ratio of 1 for the Gaussian model and a ratio of 2.13 for the
628 exponential model). However, the Gaussian model leads to smaller coefficients of variation of the
629 geostatistical parameters (up to a factor of 2.5 for the scale parameter of trajectory $\log(C_{sa})$ 1).

630 Second, the majority of the practical range estimates do not meet the interpretability criterion (see
631 2.2.5). All of the estimates of r_{95} made on the $\log(D_a)$ trajectories as well as the estimate made on
632 the $\log(C_{sa})$ 2 trajectories are indeed of the order of 30 cm, which is the minimum spacing
633 between measurements.

634 Therefore, only the estimates made on the $\log(C_{sa})$ 1 trajectory are retained. The estimated practical
635 range is indeed 50 to 63 cm depending on the chosen covariance model, exponential or Gaussian
636 (i.e., a ratio r_{95}/L of 0.05 to 0.07). The latter can then be preferred *a priori* because of its minimal
637 ER even if exponential model is close.

638 Thus, due to the too large spacing between measurement points compared to the hidden value of their
639 practical range, the question of whether the SV of the scattering parameters is a function of the
640 exposure conditions cannot be answered here.

641 Furthermore, the interpretable estimates of practical ranges differ significantly from the 1 to 2 m
642 values estimated by (O'Connor & Kenshel, 2013) on a bridge exposed to chloride ion penetration.
643 Such a difference can be explained by the fact that these authors significantly enriched their initial
644 kriging database (number of points multiplied by 7) before producing their estimates, which may have
645 influenced them significantly.

646 **6. Conclusion**

647 In this paper, a new database is proposed for analysis of the spatial variability of chloride ingress into
648 concrete. A total of 460 measurements was available, belonging to 2 exposures zones: 12 trajectories
649 of 21 points for each profile on the Internal side (sheltered from wetting-drying cycles) and 13
650 trajectories of 16 points on the External side. This data base was uses to analyze the spatial variability
651 of (i) chloride content, (ii) parameters of a model of chloride diffusion. The analysis is performed on
652 the basis of a complete framework (SCAP-1D) which raises, rigorously for the first time, questions
653 of stationarity, marginal distribution and auto-correlation.

654 The application to the total chloride content data showed that:

- 655 • the measurement error on total chloride content is negligible for the estimation of their spatial
656 variability;
- 657 • near the surface, spatio-temporally random physico-chemical and environmental phenomena
658 contribute to the diffusion and convection of chlorides so that, in coherence with the central limit
659 theorem, total chloride content at the surface can be considered totally random;
- 660 • in depth (from about 2 cm), total chlorides diffusion and fixation gradually take precedence over
661 their distribution within the coating, so that fixation and diffusion properties of concrete become
662 predominant compared to the external and surface phenomena. Total chloride content is then
663 spatially correlated with an estimated general practical range of 71 cm (scale parameter of 24 cm)
664 which is of the same order as the conventional vibration spacing during concrete pouring (30-60
665 cm (Guiraud, 2018; SETRA, 2005, p. 199)). This supports the fact that total chloride content
666 spatial correlation in depth is strongly related to the homogeneity properties of the concrete
667 resulting from pouring.

668 The application to the identification of diffusion parameters showed that:

669 The application to the chloride diffusion parameters data was presented in section 5. It allowed
670 estimation of geostatistical parameters only for the logarithm of the average surface chlorides
671 concentration. This is due to a limited number of points per trajectory (from 16 to 21) and a too large

672 spacing between measurement points (30 cm). The estimated practical range value is nevertheless
673 consistent with that of the total chloride content in depth since it is between 50 and 63 cm.
674 Implementation of SCAP-1D on these two datasets allowed to note that when the number of points
675 per trajectory is limited but not small (≥ 20), it is more efficient to first consider the results of
676 statistical tests performed on the standardized trajectory from the empirical covariance matrix, and
677 then in a second step those performed on the standardized trajectory from the modeled covariance
678 matrix. This allows to first assess the validity of the mean model, then those of the marginal density
679 model and the estimates of the geostatistical parameters of the source Random Field. On the contrary,
680 when the number of points per trajectory is small (< 20), it is preferable to consider only the results
681 of the statistical tests performed on the standardized trajectory from the modeled covariance matrix,
682 in order to guarantee its positivity of the latter.

683

684 **7. Appendix – Detailed tables of estimation process data**

685 *Table 5- Definition of trajectories and proportion of kriged data per trajectory – Ext side and Int side*

kriged data - Ex side				kriged data - Int side			
trajectory	depth (mm)	number	percentage	trajectory	depth (mm)	number	percentage
1	2.5	0	0%	16	2.5	0	0%
2	7.5	0	0%	17	7.5	1	5%
3	12.5	0	0%	18	12.5	1	5%
4	17.5	0	0%	19	17.5	1	5%
5	22.5	0	0%	20	22.5	2	10%
6	27.5	0	0%	21	27.5	1	5%
7	32.5	0	0%	22	32.5	2	10%
8	37.5	2	13%	23	37.5	2	10%
9	42.5	3	19%	24	42.5	4	19%
10	47.5	4	25%	25	47.5	3	14%
11	55	1	6%	26	55	4	19%
12	65	1	6%	27	65	4	19%
13	75	3	19%	28	75	9	43%
14	85	9	56%	29	85	15	71%
15	95	10	63%	30	95	17	81%
Total		33	14%	Total		66	21%

686 *Table 6 - Estimation of geostatistical parameters of total chloride concentration trajectories by SCAP-1D -*
 687 *model a*

trajectory		model		Σexp-tests				Σmod-tests				estimates (data multiplied by k=10e4)					Coefficient of Variation (CoV)							
#	Side	z (mm)	Npts	model	cov	reg	chg	chi2	KS	KPSS	DF	chi2	KS	KPSS	DF	μ	s	t	a	r95	CoV μ	CoV s	CoV t	CoV a
1	Ext	2,5	16	GW	expon	0	0	0	0	0	1	0	0	0	1	18,66	19,63	0,00	0,01	0,03	NaN	NaN	NaN	NaN
2	Ext	7,5	16	GW	expon	0	0	0	0	0	1	0	0	0	1	25,86	64,36	0,00	0,00	0,00	2,0E-01	1,2E+00	5,7E-01	1,7E+00
3	Ext	12,5	16	GW	expon	0	0	1	0	1	0	0	0	0	1	40,04	49,27	36,47	2,57	6,28	1,2E-01	8,9E-01	5,3E-01	1,3E+00
4	Ext	17,5	16	GW	expon	0	0	0	0	0	1	0	0	1	1	41,59	91,14	0,00	0,01	0,01	5,7E-02	7,6E+02	1,8E+02	3,8E+05
5	Ext	22,5	16	GW	expon	0	0	0	0	1	0	0	0	1	1	39,44	96,31	0,00	0,01	0,01	NaN	NaN	NaN	NaN
6	Ext	27,5	16	GW	expon	0	0	1	0	0	1	0	0	0	1	36,65	53,47	0,00	0,52	1,55	NaN	NaN	NaN	NaN
7	Ext	32,5	16	GW	expon	0	0	1	0	0	1	0	0	0	1	34,95	59,57	0,00	0,32	0,96	NaN	NaN	NaN	NaN
8	Ext	37,5	16	GW	expon	0	0	0	0	0	1	0	0	0	1	30,95	62,31	0,00	0,37	1,12	NaN	NaN	NaN	NaN
9	Ext	42,5	16	GW	expon	0	0	0	0	0	1	0	0	0	1	29,20	18,89	7,15	2,17	5,80	9,1E-02	7,5E-01	7,5E-01	1,1E+00
10	Ext	47,5	16	GW	expon	0	0	0	0	0	1	0	0	0	1	27,69	19,49	0,00	0,71	2,12	NaN	NaN	NaN	NaN
11	Ext	55	16	GW	expon	0	0	0	0	0	1	0	0	0	1	20,98	16,46	0,00	0,01	0,02	NaN	NaN	NaN	NaN
12	Ext	65	16	GW	expon	0	0	1	1	1	0	0	0	0	1	18,89	11,95	0,00	0,01	0,03	4,6E-02	1,5E+02	9,6E+09	5,6E+05
13	Ext	75	16	GW	expon	0	0	0	0	0	1	0	0	0	1	18,61	8,47	0,00	0,01	0,03	3,9E-02	1,9E+02	9,0E+09	1,5E+05
14	Int	2,5	21	GW	expon	0	0	NaN	NaN	NaN	NaN	NaN	NaN	NaN	NaN	NaN	NaN	NaN	NaN	NaN	NaN	NaN	NaN	NaN
15	Int	7,5	21	GW	expon	0	0	0	0	0	1	0	0	0	1	22,94	135,81	0,00	0,00	0,00	NaN	NaN	NaN	NaN
16	Int	12,5	21	GW	expon	0	0	1	1	0	0	0	0	0	1	40,27	38,35	111,41	3,19	5,21	1,2E-01	1,3E+00	3,6E-01	1,5E+00
17	Int	17,5	21	GW	expon	0	0	0	0	0	1	0	0	0	1	53,50	180,15	0,00	0,00	0,00	NaN	NaN	NaN	NaN
18	Int	22,5	21	GW	expon	0	0	0	0	0	1	0	0	0	1	55,01	150,55	0,00	0,34	1,01	6,5E-02	1,1E+00	1,8E+07	1,0E+00
19	Int	27,5	21	GW	expon	0	0	0	0	0	1	0	0	0	1	50,09	154,45	0,00	0,24	0,72	6,5E-02	1,8E+00	3,2E+05	1,1E+00
20	Int	32,5	21	GW	expon	0	0	0	0	0	1	0	0	0	1	47,18	168,62	0,00	0,31	0,93	7,8E-02	9,9E-01	8,2E+07	8,8E-01
21	Int	37,5	21	GW	expon	0	0	0	0	0	1	0	0	0	1	39,46	126,85	4,31	0,09	0,26	6,4E-02	2,6E+01	7,8E+02	7,8E+00
22	Int	42,5	21	GW	expon	0	0	0	0	1	0	0	0	0	1	39,57	103,23	2,06	0,29	0,86	7,2E-02	1,2E+00	5,9E+01	1,1E+00
23	Int	47,5	21	GW	expon	0	0	1	0	0	1	0	0	0	1	34,59	72,53	0,00	0,35	1,06	7,3E-02	9,4E-01	2,7E+07	8,5E-01
24	Int	55	21	GW	expon	0	0	0	0	0	1	0	0	0	1	26,46	28,31	0,00	0,00	0,00	NaN	NaN	NaN	NaN
25	Int	65	21	GW	expon	0	0	0	0	0	1	0	0	0	1	24,73	25,35	0,00	0,25	0,74	5,4E-02	1,9E+00	6,9E+05	1,2E+00

GW : Gaussian + additive white noise; reg : regression degree of mean model; chg : maximum number of changepoints of mean model

689 *Table 7 - Estimation of geostatistical parameters of the logarithm of total chloride concentration trajectories*
 690 *by SCAP-1D – model b*

trajectory				model			Σexp-tests				Σmod-tests				estimates (logarithm of data)			Coefficients of Variation (CoV)			
#	Face	z (mm)	Npts	modèle	cov	reg	chg	chi2	KS	KPSS	DF	chi2	KS	KPSS	DF	μ	s	a	CoV μ	CoV s	CoV a
1	Ext	2,5	16	G	expon	0	0	0	1	0	1	0	0	0	1	6,31	0,05	0,00	NaN	NaN	NaN
2	Ext	7,5	16	G	expon	0	0	0	1	1	1	0	0	0	1	6,04	0,08	0,52	1,6E-02	4,2E-01	7,5E-01
3	Ext	12,5	16	G	expon	0	0	0	0	0	1	0	0	1	1	5,54	0,06	0,26	1,3E-02	3,7E-01	8,4E-01
4	Ext	17,5	16	G	expon	0	0	0	0	0	1	0	0	1	1	5,51	0,05	0,00	1,0E-02	3,5E-01	1,8E+06
5	Ext	22,5	16	G	expon	0	0	0	0	1	1	0	0	1	1	5,57	0,07	0,13	1,2E-02	3,5E-01	1,6E+00
6	Ext	27,5	16	G	expon	0	0	0	0	1	1	0	0	0	1	5,63	0,05	0,47	1,3E-02	4,0E-01	6,4E-01
7	Ext	32,5	16	G	expon	0	0	0	1	1	1	0	0	0	1	5,68	0,05	0,25	1,1E-02	3,7E-01	9,4E-01
8	Ext	37,5	16	G	expon	0	0	0	0	0	1	0	0	0	1	5,81	0,06	0,40	1,4E-02	3,9E-01	6,7E-01
9	Ext	42,5	16	G	expon	0	0	0	1	1	0	0	0	0	1	5,86	0,03	0,93	1,3E-02	4,8E-01	6,5E-01
10	Ext	47,5	16	G	expon	0	0	0	1	1	1	0	0	0	1	5,90	0,03	0,69	1,1E-02	4,6E-01	7,2E-01
11	Ext	55	16	G	expon	0	0	0	0	0	1	0	0	0	1	6,19	0,05	0,02	8,7E-03	3,5E-01	4,8E+02
12	Ext	65	16	G	expon	0	0	0	0	0	1	0	0	0	1	6,29	0,04	0,01	NaN	NaN	NaN
13	Ext	75	16	G	expon	0	0	0	0	0	1	0	0	0	1	6,30	0,03	0,01	6,5E-03	3,5E-01	2,0E+05
14	Int	2,5	21	G	expon	0	0	0	0	1	1	0	0	0	1	6,18	0,05	0,00	NaN	NaN	NaN
15	Int	7,5	21	G	expon	0	0	0	0	1	1	0	0	0	1	6,19	0,21	0,00	NaN	NaN	NaN
16	Int	12,5	21	G	expon	0	0	0	0	1	1	0	0	1	1	5,58	0,14	0,01	1,5E-02	3,1E-01	1,5E+05
17	Int	17,5	21	G	expon	0	0	0	0	1	1	0	0	0	1	5,26	0,06	0,16	1,1E-02	3,1E-01	7,8E-01
18	Int	22,5	21	G	expon	0	0	0	1	1	0	0	0	0	1	5,23	0,05	0,34	1,2E-02	3,4E-01	5,3E-01
19	Int	27,5	21	G	expon	0	0	0	1	1	0	0	0	0	1	5,32	0,05	0,28	1,2E-02	3,3E-01	5,8E-01
20	Int	32,5	21	G	expon	0	0	0	1	1	0	0	0	0	1	5,39	0,06	0,28	1,3E-02	3,3E-01	6,0E-01
21	Int	37,5	21	G	expon	0	0	0	1	1	0	0	0	0	1	5,58	0,08	0,13	1,2E-02	3,1E-01	1,0E+00
22	Int	42,5	21	G	expon	0	0	0	0	1	1	0	0	0	1	5,57	0,07	0,28	1,3E-02	3,3E-01	5,7E-01
23	Int	47,5	21	G	expon	0	0	0	1	1	0	0	0	0	1	5,70	0,06	0,30	1,2E-02	3,3E-01	5,7E-01
24	Int	55	21	G	expon	0	0	0	0	1	1	0	0	0	1	5,95	0,04	0,19	7,9E-03	3,1E-01	6,4E-01
25	Int	65	21	G	expon	0	0	0	0	1	1	0	0	0	1	6,02	0,04	0,24	8,4E-03	3,2E-01	5,9E-01

G : Gaussian; reg : regression degree of mean model; chg : maximum number of changepoints of mean model

691

692 *Table 8 - Computation of the evidence ratios associated with the exponential and Gaussian covariance*
 693 *models for model b using the corrected Akaike criterion*

trajectory				model			Corrected Akaike criteria		Evidence Ratios	
#	Face	z (mm)	Npts	model	reg	chg	cov gauss	cov expon	cov gauss	cov expon
17	Int	17,5	21	G	0	0	-3.21E+01	-3.22E+01	1.04	1.00
18	Int	22,5	21	G	0	0	-3.89E+01	-3.89E+01	1.00	1.05
19	Int	27,5	21	G	0	0	-3.59E+01	-3.55E+01	1.00	1.21
20	Int	32,5	21	G	0	0	-3.05E+01	-3.07E+01	1.11	1.00
21	Int	37,5	21	G	0	0	-2.39E+01	-2.39E+01	1.00	1.01
22	Int	42,5	21	G	0	0	-2.89E+01	-2.94E+01	1.29	1.00
23	Int	47,5	21	G	0	0	-3.14E+01	-3.18E+01	1.18	1.00
24	Int	55	21	G	0	0	-4.21E+01	-4.18E+01	1.00	1.14
25	Int	65	21	G	0	0	-4.22E+01	-4.18E+01	1.00	1.26

G : gaussian

694

695

696 **8. Acknowledgment**

697 The authors would like to thank all the partners of iMAREO2 project: Keops Automation (D. Follut,
698 D. Olivier), Université de Nantes (M. Roche), Nantes—Saint Nazaire Port (P. Lijour, M. Labegorre).
699 The authors would like to thank the Pays de la Loire region for its financial support.

700 **9. References**

- 701 Angst, U., Elsener, B., Larsen, C. K., & Vennesland, Ø. (2009). Critical chloride content in
702 reinforced concrete—A review. *Cement and Concrete Research*, 39(12), 1122–1138.
703 <https://doi.org/10.1016/j.cemconres.2009.08.006>
- 704 Arnaud, M., & Emery, X. (2000). *Estimation et interpolation spatiale: Méthodes déterministes et*
705 *méthodes géostatistiques*. Hermès. <http://agritrop.cirad.fr/487412/>
- 706 Baillargeon, S. (2005). *Le Krigeage*. Faculté des sciences et de génie UNIVERSITÉ LAVAL
707 QUÉBEC. https://archimede.mat.ulaval.ca/theses/S-Baillargeon_05.pdf
- 708 Bastidas-Arteaga, E., & Schoefs, F. (2015). Sustainable maintenance and repair of RC coastal
709 structures. *Proceedings of the ICE-Maritime Engineering*, 168(4), 162–173.
- 710 Biondi, L., Perry, M., McAlorum, J., Vlachakis, C., Hamilton, A., & Lo, G. (2021). Alkali-
711 Activated Cement Sensors for Sodium Chloride Monitoring. *IEEE Sensors Journal*, 21(19),
712 21197–21204. <https://doi.org/10.1109/JSEN.2021.3100582>
- 713 Bonnet, S., Schoefs, F., & Salta, M. (2017). Sources of uncertainties for total chloride profile
714 measurements in concrete: Quantization and impact on probability assessment of corrosion
715 initiation. *European Journal of Environmental and Civil Engineering*, 1–16.
716 <https://doi.org/10.1080/19648189.2017.1375997>
- 717 Bourreau, L., Bouteiller, V., Schoefs, F., Gaillet, L., Thauvin, B., Schneider, J., & Naar, S. (2019).
718 Uncertainty assessment of concrete electrical resistivity measurements on a coastal bridge.
719 *Structure and Infrastructure Engineering*, 1–11.
720 <https://doi.org/10.1080/15732479.2018.1557703>
- 721 Bourreau, L., Gaillet, L., Bouteiller, V., Schoefs, F., Thauvin, B., Schneider, J., & Naar, S. (2020).
722 Spatial identification of exposure zones of concrete structures exposed to a marine
723 environment with respect to reinforcement corrosion. *Structure and Infrastructure*
724 *Engineering*, 16(2), 346–354. <https://doi.org/10.1080/15732479.2019.1655072>
- 725 BS 6349-1:2000. (2000). *Maritime structures. Code of practice for general criteria* [Norme].
726 <https://shop.bsigroup.com/ProductDetail/?pid=000000000030055558>

- 727 Burnham, K. P., & Anderson, D. R. (2010). *Model selection and multimodel inference: A practical*
728 *information-theoretic approach* (2. ed., [4. printing]). Springer.
- 729 Chilès, J.-P., & Delfiner, P. (2012). *Geostatistics: Modeling spatial uncertainty* (2. ed). Wiley.
- 730 Clerc, R., Oumouni, M., & Schoefs, F. (2019). SCAP-1D: A Spatial Correlation Assessment
731 Procedure from unidimensional discrete data. *Reliability Engineering & System Safety*, *191*,
732 106498. <https://doi.org/10.1016/j.ress.2019.106498>
- 733 Cressie, N. A. C. (1993). *Statistics for spatial data* (Rev. ed). Wiley.
- 734 Der Kiureghian, A., & Ke, J.-B. (1987). The stochastic finite element method in structural
735 reliability. In Y. K. Lin, G. I. Schuëller, & P. Spanos (Eds.), *Stochastic Structural*
736 *Mechanics* (pp. 84–109). Springer Berlin Heidelberg.
- 737 Dickey, D. A., & Fuller, W. A. (1981). Likelihood Ratio Statistics for Autoregressive Time Series
738 with a Unit Root. *Econometrica*, *49*(4), 1057. <https://doi.org/10.2307/1912517>
- 739 Englund, S., & Sørensen, J. D. (1998). A probabilistic model for chloride-ingress and initiation of
740 corrosion in reinforced concrete structures. *Structural Safety*, *20*(1), 69–89.
- 741 Fares, M., Villain, G., Bonnet, S., Palma Lopes, S., Thauvin, B., & Thiery, M. (2018). Determining
742 chloride content profiles in concrete using an electrical resistivity tomography device.
743 *Cement and Concrete Composites*, *94*, 315–326.
744 <https://doi.org/10.1016/j.cemconcomp.2018.08.001>
- 745 Glasser, F. P., Marchand, J., & Samson, E. (2008). Durability of concrete—Degradation phenomena
746 involving detrimental chemical reactions. *Cement and Concrete Research*, *38*(2), 226–246.
747 <https://doi.org/10.1016/j.cemconres.2007.09.015>
- 748 Gomez-Cardenas, C., Sbartai, Z. M., Balayssac, J. P., Garnier, V., & Breysse, D. (2015). New
749 optimization algorithm for optimal spatial sampling during non-destructive testing of
750 concrete structures. *Engineering Structures*, *88*, 92–99.
751 <https://doi.org/10.1016/j.engstruct.2015.01.014>
- 752 Guiraud, P. (2018, April). Vibration des bétons. *Infociments*.
753 <https://www.infociments.fr/betons/vibration-des-betons>
- 754 Hill, R. (1963). Elastic properties of reinforced solids: Some theoretical principles. *Journal of the*
755 *Mechanics and Physics of Solids*, *11*(5), 357–372. [https://doi.org/10.1016/0022-](https://doi.org/10.1016/0022-5096(63)90036-X)
756 [5096\(63\)90036-X](https://doi.org/10.1016/0022-5096(63)90036-X)
- 757 Hunkeler, D. F., Ungricht, H., & Deillon, F. (2000). *Determination of the chloride content of*
758 *concrete and execution of a Round Robin test in two steps* (VSS No. 546). Eidg.
759 Departement für Umwelt, Verkehr, Energie und Kommunikation (UVEK), Bundesamt für
760 Strassen.

761 <https://www.tfb.ch/Htdocs/Files/v/8671.pdf/Publikationsliste/ChloridbestimmungRingversu>
762 [chBerichtVSSNr.5462000.pdf](https://www.tfb.ch/Htdocs/Files/v/8671.pdf/Publikationsliste/ChloridbestimmungRingversu)

763 Johnson, N. L., Balakrishnan, N., & Kotz, S. (1995). *Continuous univariate distributions. Vol.2*
764 (2ed.). Wiley.

765 Karimi, A. R. (2002). *Probabilistic assessment of deterioration and strength of concrete bridge*
766 *beams and slabs* [Imperial College London].
767 <https://ethos.bl.uk/OrderDetails.do?uin=uk.bl.ethos.540519>

768 Kaushik, S. K., & Islam, S. (1995). Suitability of sea water for mixing structural concrete exposed
769 to a marine environment. *Cement and Concrete Composites*, 17(3), 177–185.
770 [https://doi.org/10.1016/0958-9465\(95\)00015-5](https://doi.org/10.1016/0958-9465(95)00015-5)

771 Killick, R., Fearnhead, P., & Eckley, I. A. (2012). Optimal Detection of Changepoints With a
772 Linear Computational Cost. *Journal of the American Statistical Association*, 107(500),
773 1590–1598. <https://doi.org/10.1080/01621459.2012.737745>

774 Kwiatkowski, D., Phillips, P. C. B., Schmidt, P., & Shin, Y. (1992). Testing the null hypothesis of
775 stationarity against the alternative of a unit root: How sure are we that economic time series
776 have a unit root? *Journal of Econometrics*, 54(1), 159–178. [https://doi.org/10.1016/0304-](https://doi.org/10.1016/0304-4076(92)90104-Y)
777 [4076\(92\)90104-Y](https://doi.org/10.1016/0304-4076(92)90104-Y)

778 Lecieux, Y., Rozière, E., Gaillard, V., Lupi, C., Leduc, D., Priou, J., Guyard, R., Chevreuil, M., &
779 Schoefs, F. (2019). Monitoring of a Reinforced Concrete Wharf Using Structural Health
780 Monitoring System and Material Testing. *Journal of Marine Science and Engineering*, 7(4),
781 84. <https://doi.org/10.3390/jmse7040084>

782 Lecieux, Y., Schoefs, F., Bonnet, S., Lecieux, T., & Lopes, S. P. (2015). Quantification and
783 uncertainty analysis of a structural monitoring device: Detection of chloride in concrete
784 using DC electrical resistivity measurement. *Nondestructive Testing and Evaluation*, 30(3),
785 216–232. <https://doi.org/10.1080/10589759.2015.1029476>

786 O'Connor, A. J., & Kenshel, O. (2013). Experimental Evaluation of the Scale of Fluctuation for
787 Spatial Variability Modeling of Chloride-Induced Reinforced Concrete Corrosion. *Journal*
788 *of Bridge Engineering*, 18(1), 3–14. [https://doi.org/10.1061/\(ASCE\)BE.1943-5592.0000370](https://doi.org/10.1061/(ASCE)BE.1943-5592.0000370)

789 Othmen, I., Bonnet, S., & Schoefs, F. (2018). Statistical investigation of different analysis methods
790 for chloride profiles within a real structure in a marine environment. *Ocean Engineering*,
791 157, 96–107. <https://doi.org/10.1016/j.oceaneng.2018.03.040>

792 Oumouni, M., & Schoefs, F. (2021a). A Perturbed Markovian process with state-dependent
793 increments and measurement uncertainty in degradation modeling. *Computer-Aided Civil*
794 *and Infrastructure Engineering*, 36(8), 978–995. <https://doi.org/10.1111/mice.12644>

795 Oumouni, M., & Schoefs, F. (2021b). Spatial variability assessment of structures from adaptive
796 NDT measurements. *Structural Safety*, 89, 102052.
797 <https://doi.org/10.1016/j.strusafe.2020.102052>

798 Priou, J., Lecieux, Y., Chevreuril, M., Gaillard, V., Lupi, C., Leduc, D., Rozière, E., Guyard, R., &
799 Schoefs, F. (2019). In situ DC electrical resistivity mapping performed in a reinforced
800 concrete wharf using embedded sensors. *Construction and Building Materials*, 211, 244–
801 260. <https://doi.org/10.1016/j.conbuildmat.2019.03.152>

802 Qu, F., Li, W., Dong, W., Tam, V. W. Y., & Yu, T. (2021). Durability deterioration of concrete
803 under marine environment from material to structure: A critical review. *Journal of Building*
804 *Engineering*, 35, 102074. <https://doi.org/10.1016/j.jobe.2020.102074>

805 Ragab, A. M., Elgammal, M. A., Hodhod, O. A., & Ahmed, T. E. (2016). Evaluation of field
806 concrete deterioration under real conditions of seawater attack. *Construction and Building*
807 *Materials*, 119, 130–144. <https://doi.org/10.1016/j.conbuildmat.2016.05.014>

808 Ravahatra, N. R., Duprat, F., Schoefs, F., de Larrard, T., & Bastidas-Arteaga, E. (2017). Assessing
809 the Capability of Analytical Carbonation Models to Propagate Uncertainties and Spatial
810 Variability of Reinforced Concrete Structures. *Frontiers in Built Environment*, 3.
811 <https://doi.org/10.3389/fbuil.2017.00001>

812 Safhi, A. el M., Benzerzour, M., Rivard, P., Abriak, N.-E., & Ennahal, I. (2019). Development of
813 self-compacting mortars based on treated marine sediments. *Journal of Building*
814 *Engineering*, 22, 252–261. <https://doi.org/10.1016/j.jobe.2018.12.024>

815 Schoefs, F., Bastidas-Arteaga, E., Tran, T. V., Villain, G., & Derobert, X. (2016). Characterization
816 of random fields from NDT measurements: A two stages procedure. *Engineering Structures*,
817 111, 312–322. <https://doi.org/10.1016/j.engstruct.2015.11.041>

818 Schoefs, F., Bastidas-Arteaga, E., & Tran, T.-V. (2017a). Optimal embedded sensor placement for
819 spatial variability assessment of stationary random fields. *Engineering Structures*, 152, 35–
820 44. <https://doi.org/10.1016/j.engstruct.2017.08.070>

821 Schoefs, F., Oumouni, M., Clerc, R., Othmen, I., & Bonnet, S. (2017b). Statistical analysis and
822 probabilistic modeling of chloride ingress spatial variability in concrete coastal
823 infrastructures. *Edition 4, Split, Croatie*, 229–234. <https://doi.org/10.5150/cmcm.2017.042>

824 Schoefs, F., Oumouni, M., Follut, D., Lecieux, Y., Gaillard, V., Lupi, C., & Leduc, D. (2022).
825 Added value of monitoring for the maintenance of a reinforced concrete wharf with spatial
826 variability of chloride content: A practical implementation. *Structure and Infrastructure*
827 *Engineering*, 0(0), 1–13. <https://doi.org/10.1080/15732479.2022.2077767>

828 Schoefs, F., Awa Zahui Raissa, K., Bonnet, S., & O’Conor, A. J. (2023). Uncertainty quantification
829 of semi-destructive testing for chloride content assessment for a concrete bridge in maritime

830 environment. *Frontiers in Built Environment*, 9.
831 <https://www.frontiersin.org/articles/10.3389/fbuil.2023.1130066>

832 SETRA. (2005). *Mémoar—Mémento pour la mise en oeuvre sur ouvrages d'art*. Cerema (ex-Setra).
833 <https://www.cerema.fr/fr/centre-ressources/boutique/memoar-memento-mise-oeuvre->
834 [ouvrages-art](https://www.cerema.fr/fr/centre-ressources/boutique/memoar-memento-mise-oeuvre-)

835 Stewart, M. G. (2004). Spatial variability of pitting corrosion and its influence on structural fragility
836 and reliability of RC beams in flexure. *Structural Safety*, 26(4), 453–470.
837 <https://doi.org/10.1016/j.strusafe.2004.03.002>

838 Stewart, M. G., & Mullard, J. A. (2007). Spatial time-dependent reliability analysis of corrosion
839 damage and the timing of first repair for RC structures. *Engineering Structures*, 29(7),
840 1457–1464. <https://doi.org/10.1016/j.engstruct.2006.09.004>

841 Stewart, M. G., & Val, D. V. (2003). Multiple Limit States and Expected Failure Costs for
842 Deteriorating Reinforced Concrete Bridges. *Journal of Bridge Engineering*, 8(6), 405–415.
843 [https://doi.org/10.1061/\(ASCE\)1084-0702\(2003\)8:6\(405\)](https://doi.org/10.1061/(ASCE)1084-0702(2003)8:6(405))

844 Torres-Luque, M., Bastidas-Arteaga, E., Schoefs, F., Sánchez-Silva, M., & Osmá, J. F. (2014).
845 Non-destructive methods for measuring chloride ingress into concrete: State-of-the-art and
846 future challenges. *Construction and Building Materials*, 68, 68–81.

847 Torres-Luque, M., Osmá, J. F., Sánchez-Silva, M., Bastidas-Arteaga, E., & Schoefs, F. (2017).
848 Chlordetect: Commercial Calcium Aluminate Based Conductimetric Sensor for Chloride
849 Presence Detection. *Sensors*, 17(9), 2099. <https://doi.org/10.3390/s17092099>

850 Vennesland, P. Ø., Climent, M. A., & Andrade, C. (2013). Recommendations of RILEM TC 178-
851 TMC: Testing and modelling chloride penetration in concrete. *Materials and Structures*, 8.
852 <https://doi.org/10.1617/s11527-012-9968-1>

853 Wasserman, L. (2004). *All of Statistics*. Springer New York. <https://doi.org/10.1007/978-0-387->
854 [21736-9](https://doi.org/10.1007/978-0-387-21736-9)

855 Watanabe, A., Tokuda, S., Mizuta, Y., Miyamoto, S., Nakanishi, T., Furukawa, H., & Minagawa,
856 H. (2021). Toward automated non-destructive diagnosis of chloride attack on concrete
857 structures by near infrared spectroscopy. *Construction and Building Materials*, 305, 124796.
858 <https://doi.org/10.1016/j.conbuildmat.2021.124796>

859 Wegian, F. M. (2010). Effect of seawater for mixing and curing on structural concrete. *The IES*
860 *Journal Part A: Civil & Structural Engineering*, 3(4), 235–243.
861 <https://doi.org/10.1080/19373260.2010.521048>

862 Zaki, A., Chai, H. K., Aggelis, D. G., & Alver, N. (2015). Non-Destructive Evaluation for
863 Corrosion Monitoring in Concrete: A Review and Capability of Acoustic Emission
864 Technique. *Sensors*, 15(8), Article 8. <https://doi.org/10.3390/s150819069>

